

Controlling VUV photon fluxes in low-pressure inductively coupled plasmas

Peng Tian and Mark J Kushner¹

Electrical Engineering and Computer Science Department, University of Michigan, 1301 Beal Ave., Ann Arbor, MI 48109-2122, USA

E-mail: tianpeng@umich.edu and mjkush@umich.edu

Received 9 March 2015, revised 16 April 2015

Accepted for publication 23 April 2015

Published 9 June 2015



CrossMark

Abstract

Low-pressure (a few to hundreds of millitorrs) inductively coupled plasmas (ICPs), as typically used in microelectronics fabrication, often produce vacuum-ultraviolet (VUV) photon fluxes onto surfaces comparable to or exceeding the magnitude of ion fluxes. These VUV photon fluxes are desirable in applications such as sterilization of medical equipment but are unwanted in many materials fabrication processes due to damage to the devices by the high-energy photons. Under specific conditions, VUV fluxes may stimulate etching or synergistically combine with ion fluxes to modify polymeric materials. In this regard, it is desirable to control the magnitude of VUV fluxes or the ratio of VUV fluxes to those of other reactive species, such as ions, or to discretely control the VUV spectrum. In this paper, we discuss results from a computational investigation of VUV fluxes from low-pressure ICPs sustained in rare gas mixtures. The control of VUV fluxes through the use of pressure, pulsed power, and gas mixture is discussed. We found that the ratio, β , of VUV photon to ion fluxes onto surfaces generally increases with increasing pressure. When using pulsed plasmas, the instantaneous value of β can vary by a factor of 4 or more during the pulse cycle due to the VUV flux more closely following the pulsed power.

Keywords: inductively coupled plasma, radiation transport, VUV, pulsed plasma

(Some figures may appear in colour only in the online journal)

1. Introduction

Low-pressure, non-equilibrium inductively coupled plasmas (ICPs) are widely used for materials processing in microelectronics fabrication [1–10]. In these materials processing applications, there has been considerable attention paid to controlling the fluxes of radicals and ions, and the distribution of ion energies onto the substrate, in order to optimize the process. Gas mixtures, power format (continuous wave (cw) or pulsed) and coil design have been investigated with the goal of having uniform fluxes of reactants of the user's choosing onto the substrate. This control is particularly important in applications where damage to the substrate may occur, for example as a result of differential charging of microelectronics features [11–13]. Less attention has been paid to vacuum-ultraviolet (VUV) photon fluxes produced by

these low-pressure plasmas and the consequences of those fluxes or the properties of materials.

Woodworth *et al* [14] measured absolute intensities of VUV emission from ICPs in the context of plasma etching of metals. They found that the total VUV intensity (95–250 nm) from a 10 mTorr Cl_2/BCl_3 plasma powered at 1100 W exceeded 0.5 mW cm^{-2} , or a flux of $5 \times 10^{14} \text{ cm}^{-2} \text{ s}^{-1}$. This emission was dominated by the resonance lines of neutral Cl at 137–138 nm. Woodworth *et al* [15] made similar measurements of VUV fluxes sustained in fluorocarbon and Ar/fluorocarbon gas mixtures at pressures to tens of millitorrs and powers of hundreds of watts. In the pure fluorocarbon gases (C_2F_6 , CHF_3 , C_4F_8), VUV fluxes in the range of 70–140 nm were $10\text{--}30 \times 10^{14} \text{ cm}^{-2} \text{ s}^{-1}$ principally from the resonance lines of neutral C and F. When diluting the fluorocarbon gases with argon (e.g. $\text{Ar}/\text{C}_2\text{F}_6 = 50/50$), the total VUV flux increased by an order of magnitude, from $11 \times 10^{14} \text{ cm}^{-2} \text{ s}^{-1}$ to $115 \times 10^{14} \text{ cm}^{-2} \text{ s}^{-1}$, due to the additional radiation resulting

¹ Author to whom any correspondence should be addressed.

from the resonance lines of Ar at 104.8 nm and 106.7 nm. In pure argon for similar conditions, the VUV fluxes increased to $3.5 \times 10^{16} \text{ cm}^{-2} \text{ s}^{-1}$. The plasma density was a few times 10^{11} cm^{-3} , producing ion fluxes onto the substrate of $3 \times 10^{16} \text{ cm}^{-2} \text{ s}^{-1}$. So VUV fluxes were comparable to the ion fluxes. Similar intensities of VUV fluxes, 10^{15} – $10^{16} \text{ cm}^{-2} \text{ s}^{-1}$, were measured by Jinnai *et al* using an on-wafer VUV sensor in ICP plasmas sustained in Ar, CF_3I , and C_4F_8 [16].

Titus *et al* [17] measured absolute fluxes of resonance radiation from Ar (104.8 and 106.7 nm) and ion fluxes from ICPs in pure Ar at pressures of 1–50 mTorr and powers of 25–400 W. They found that at all pressures, the VUV flux increased linearly with power with a maximum value of $1.5 \times 10^{16} \text{ cm}^{-2} \text{ s}^{-1}$ at 1 mTorr and 400 W. In general, the VUV flux was approximately one-half the ion flux.

Investigating VUV emission and its control in ICPs is motivated from at least four perspectives. The first is the damage to microelectronics materials resulting from VUV fluxes during processing. For example, films with ultra-low dielectric constant, such as porous SiOCH , are used as the interlayer dielectric in interconnect wiring in microelectronics devices, and can be damaged by VUV photons during plasma etching [18, 19]. Bond breaking by VUV photons and subsequent water uptake into the film increases its dielectric constant. The second includes synergistic effects that result from simultaneous fluxes of VUV photons and ion bombardment. For example, the roughening of photoresist has different characteristics as a function of temperature depending on whether the film receives only ion fluxes or fluxes of both ions and VUV photons [20, 21]. The third includes photon-stimulated processes. Recent measurements have shown that VUV photon fluxes from ICPs onto halogen-passivated silicon can produce etching when the energies of the ion fluxes are below the accepted thresholds for ion-produced etching [22]. The last perspective concerns the use of VUV fluxes from low-pressure ICPs for sterilization of medical equipment [23].

These observations motivate the development of methods to independently control VUV photon fluxes or to control the ratio of VUV fluxes to ion fluxes in ICPs used for materials processing. This optimization is complicated by the dynamics of resonant radiation transport in low-pressure plasmas. It is well understood that resonant photons in plasmas may undergo many absorptions and re-emissions between the site of initial emission and leaving the plasma. This process of absorption and re-emission is known as *radiation trapping* and has the overall effect of lengthening the effective lifetime of the excited state as observed from outside the plasma [24]. This extended lifetime is expressed as a radiation trapping factor—the ratio of the effective lifetime including reabsorption to the natural lifetime of the excited state. At high pressures, the trapping factor can be 10^4 or larger, resulting in the resonant radiative excited state being effectively metastable. The photons that do escape the plasma tend to be at frequencies in the wings of the optical lineshape function where the likelihood for absorption (and emission) is small compared to line center. The flux of photons that do escape the plasma are a small fraction of total photon flux in the middle of the plasma due to absorption and re-emission. For radiation transport that

is heavily trapped, the vast majority of photons are emitted, absorbed, and re-emitted many thousands of times before escaping the plasma.

In this paper, we discuss results from a computational investigation of VUV fluxes produced in low-pressure (tens of millitorrs) cw and pulsed ICPs sustained in Ar, Ar/Xe, and He/Ar gas mixtures. The goal of this investigation is to characterize the VUV fluxes and propose methods to control the absolute value of VUV fluxes, their spectra and the ratio of VUV fluxes to ion fluxes. We found that in cw ICPs sustained in Ar at constant power, VUV fluxes onto the bottom substrate are a function of gas pressure with an asymptotic constant, maximum VUV fluxes being produced at high pressures. This result, though, is a function of the geometry and aspect ratio of the plasma chamber. Ion fluxes onto the bottom substrate, on the other hand, monotonically decreased with increasing pressure. In pulsed Ar ICPs, the cycle-averaged VUV fluxes increase as the duty cycle increases, while ion fluxes are less sensitive to changes of duty cycle. This scaling then provides a means to control the ratio of photon to ion fluxes by duty cycle. When rare-gas mixtures are used, some coarse tuning of the VUV emission spectrum is possible through the mole fractions of the rare gases. However, the proportion of VUV flux from each component is highly non-linear. For example, in Ar/Xe mixtures, the VUV fluxes from Xe exceed those from Ar when the mole fraction of Xe exceeds 20%. In He/Ar mixtures, the VUV flux from Ar dominates until the He mole fraction exceeds 99%.

The model used in this investigation is described in section 2, followed by a short discussion of the plasma dynamics of ICPs in section 3, including validation of the model. The scaling of VUV fluxes are discussed in sections 4 and 5 followed by our concluding remarks in section 6.

2. Description of the model

The model used in this investigation is the Hybrid Plasma Equipment Model (HPEM), which is described in detail in [25]. Briefly, the HPEM is a modular simulator in which different physical processes are addressed in an iterative manner. In this investigation, the major modules used in the HPEM are the Electromagnetics Module (EMM), the electron Monte Carlo Simulation (eMCS) within the Electron Energy Transport Module (EETM), the Fluid Kinetics Module (FKM), and the Radiation Transport Module (RTM). The densities of all charged and neutral species, and the electric potential, are obtained from the FKM. Separate continuity, momentum, and energy equations are integrated in time for all heavy particles. The electron density is obtained from integrating a continuity equation with fluxes provided by the Sharffeter–Gummel formulation which analytically provides upwind or downwind fluxes [26]. The electric potential is obtained by a semi-implicit solution of Poisson's equation. Charge densities are computed on surfaces as being due to the fluxes of electrons and ions from the bulk plasma, secondary electrons leaving the surface, and secondary electrons from other locations collected by those surfaces. Inductively coupled electromagnetic fields are produced by the EMM using

a frequency domain solution of Maxwell's equations which provides a stationary wave equation. Given the symmetry of the reactor (here, cylindrical), the inductively coupled electric fields are in the azimuthal direction, and the magnetic fields are in the (r, z) plane. The calculation provides the amplitudes and phase angles of each field.

The eMCS is used for both the bulk electron energy transport and the transport of sheath-accelerated beam electrons, and is described in detail in [27]. Electrostatic fields from the FKM and electromagnetic fields from the EMM are used to advance trajectories of pseudoparticles in the eMCS. A particle-mesh technique is used to resolve electron–electron collisions. Statistics for the positions and energies of electrons are recorded to produce electron energy distributions (EEDs), which are then combined with the electron densities from the FKM to produce electron impact sources as a function of position.

The eMCS is also used to compute separate source functions resulting from secondary electrons emitted from surfaces. The secondary electrons are produced by fluxes of ions, excited states, and photons. The fluxes of ions and excited states are obtained from the FKM. The fluxes of photons are obtained from the RTM. Secondary electrons that fall in energy below the minimum inelastic threshold are removed from the eMCS for secondary electrons and used as source functions in the bulk electron continuity equation. Secondary electrons collected on surfaces are included as sources of negative charge in the solution of surface charge densities in the FKM.

The plasma conditions we investigated are at low enough pressures that the electromagnetic skin depth may be anomalous [28–30]. To better represent the power deposition under these conditions the following technique was used. During the eMCS, the total power absorbed by electrons is computed by integrating the trajectories of the electron pseudoparticles in the electromagnetic field,

$$P_a = \frac{1}{\tau} \int_0^\tau \sum_i q w_i (\vec{v}_i \cdot \vec{E}) dt, \quad (1)$$

where P_a is the absorbed power, the integral is over the rf period τ , the summation is over pseudoparticles representing w_i electrons per particle having velocity \vec{v}_i , and \vec{E} is the electric field at the location of the particle. P_a is then used to normalize the antenna currents and thus the magnitudes of the electromagnetic fields calculated in the EMM to deliver the desired power. In prior studies, we found this technique provided essentially the same plasma properties as computing plasma currents in the eMCS and using those currents in solving of Maxwell's equations [31].

For cw plasmas, these modules are iterated (typically, in the order of EMM, EETM, FKM, RTM) until a quasi-steady state is achieved. The time spent in any given module is selected for numerical stability and to minimize artificial transients that may occur due to changes in, for example, source functions due to updates from the EETM. Acceleration techniques may be used to speed numerical convergence. For pulsed plasmas, the time spent in each module and the frequency of iteration are chosen to resolve the transients.

Radiation transport in the RTM is addressed using Monte Carlo techniques [24, 32, 33]. Photon pseudoparticles are isotropically launched from locations in the plasma weighted by the densities of the radiating states, for example Ar($1s_4$) and Ar($1s_2$) in the case of argon plasmas. The photon pseudoparticles are advanced in line-of-sight trajectories until the pseudoparticles hit a surface, are resonantly absorbed by ground state Ar or are nonresonantly absorbed through, for example, photoionization of excited states. The absorbed quanta of energy represented by the pseudoparticles are then either re-radiated assuming partial frequency redistribution [34, 35] or quenched. By quenching, we mean that the quantum of energy resident in the excited state undergoes a collision (e.g. electron impact ionization or super-elastic relaxation, Penning ionization) prior to that quantum of energy being re-radiated as a photon. The lineshape function of the emitted photons follows a Voigt profile using the local gas temperature and collision frequency to determine broadening. The fluxes of photon pseudoparticles are recorded as a function of position in the gas phase and on surfaces. The fluxes in the gas phase are used to produce photoionization sources used in the FKM. The fluxes striking surfaces are used for sources of secondary electrons by photoelectron emission, and also represent the optical output of the plasma. The details of the RTM follow.

The RTM tracks quanta of photons that are initially emitted in proportion to excited state densities. For any given run of the RTM, a probability array is constructed which provides the mean free path for absorption of a photon emitted from transition i as a function of position and frequency.

$$\lambda_i(\vec{r}, \nu) = \left[\sum_j N_j(\vec{r}) \sigma_{0j} g_j(\vec{r}, \nu) + \sum_k N_k(\vec{r}) \sigma_{ik} \right]^{-1}. \quad (2)$$

In equation (2), the first sum accounts for resonant absorption by species j having density $N_j(\vec{r})$, line-center absorption cross section σ_{0j} and Voigt lineshape function $g_j(\vec{r}, \nu)$. The spatial dependence of the lineshape function comes through the possible spatial dependence of gas temperature and collision frequency. The sum over species for resonant absorption accounts for closely spaced transitions, as might occur for hyperfine splitting and isotopes. The second sum accounts for nonresonant absorption of photon i by species k having density $N_k(\vec{r})$ with cross section σ_{ik} , as might occur in photoionization. The minimum mean free path in the plasma is then determined by $\lambda_{im}(\nu) = \min[\lambda_i(\vec{r}, \nu)]$.

Another array is constructed for the frequency of quenching collisions of the excited state that produces a photon from transition i ,

$$f_{Qi}(\vec{r}, \nu) = \sum_m N_m(\vec{r}) k_{Qmi}(\vec{r}) \quad (3)$$

where the sum is over collisions with species m having density N_m that quenches the excited state producing photon i with rate coefficient k_{Qmi} . A third array is constructed, f_{Ni} , which is analogous to f_{Qi} but which accounts for nonquenching but broadening or velocity-changing collisions having rate coefficient $k_{Nmi}(\vec{r})$.

The optical frequency of the initially emitted pseudoparticle for the photon from transition i emitted at \vec{r} is randomly chosen from $g_i(\vec{r}, \nu)$ using the following procedure. The Voigt profile can be reduced to a function that depends on the ratio of the homogeneous linewidth, $\Delta\nu_H$, and the inhomogeneous linewidth, which in this case is the Doppler linewidth, $\Delta\nu_D$,

$$g_i(\vec{r}, \nu) = \frac{\gamma_i(\vec{r})}{\pi^{3/2}} \int_{-\infty}^{\infty} \frac{e^{-y^2}}{\gamma(\vec{r})^2 + (\nu_i'(\vec{r}) - y)^2} dy, \quad \gamma_i(\vec{r}) = \frac{\Delta\nu_{iH}(\vec{r})}{2\Delta\nu_{iD}(\vec{r})}, \quad \nu_i'(\vec{r}) = \frac{\nu - \nu_{i0}}{\Delta\nu_{iD}(\vec{r})}, \quad (4)$$

where ν_{i0} is the absolute line center for transition i and $\Delta\nu_{iH}$ is the sum of the natural decay rate for photon i given by the Einstein coefficient A_i and the sum of the rate of broadening collisions with species m ,

$$\Delta\nu_{iH}(\vec{r}) = \frac{1}{2\pi}(A_i + A_l + 2f_{Qi}(\vec{r}, \nu)). \quad (5)$$

A_l is the natural decay rate of the lower level of the transition which for resonant radiation is zero. The Doppler linewidth is

$$\Delta\nu_{iD}(\vec{r}) = \left(\frac{8k_B T_i(\vec{r}) \ln 2}{M_i c^2} \right)^{1/2} \nu_{i0} \quad (6)$$

where $T_i(\vec{r})$ is the temperature of the atom emitting photon i having mass M_i (k_B is Boltzmann's constant and c is the speed of light). Since the calculation of $g_i(\vec{r}, \nu)$ is computationally expensive and its value is required frequently, $g_i(\vec{r}, \nu)$ is precomputed and recorded in an array spanning a specified number of Doppler widths, typically 8–10. The initial emission frequency of a photon ν_k is the frequency value that satisfies

$$\frac{1}{G} \sum_{m=1}^{k-1} g_i(\vec{r}, \nu_m) \Delta\nu_m < \rho < \frac{1}{G} \sum_{m=1}^k g_i(\vec{r}, \nu_m) \Delta\nu_m, \quad G = \sum_m g_i(\vec{r}, \nu_m) \Delta\nu_m \quad (7)$$

where ρ is a random number distributed on (0, 1), the sums are over frequency bins in the $g_i(\vec{r}, \nu)$ array, G is the sum over all bins in the array and $\Delta\nu_m$ is the frequency width of the m th bin. Note that for every process requiring a random number ρ a separate independent random number generator sequence is used. The direction of the photon is uniformly randomly selected from 4π steradians. A mean free path for absorption of the photon, $\lambda' = -\lambda_{im}(\nu) \ln(\rho)$, is randomly selected from $\lambda_{im}(\nu)$. The pseudoparticle is given a weighting $w_i(\vec{r})$ representing the number of photons emitted per second in the optical transition i from \vec{r} . This weighting is

$$w_i(\vec{r}) = \frac{N_i(\vec{r}) A_i \Delta V(\vec{r})}{n_i(\vec{r})} \quad (8)$$

where $\Delta V(\vec{r})$ is the volume of the numerical cell from which the photon is emitted and $n_i(\vec{r})$ is the number of pseudoparticles emitted from that location, described below. The photon's initial position in the numerical mesh representing the reactor geometry is randomly distributed in 3D. The emission

is assumed to have occurred after a randomly selected lifetime of the excited state, $\tau_i = -A_i^{-1} \ln(\rho)$. A tally of the cumulative lifetime of the quantum of energy carried by the photon is initialized with $\tau_{Ci} = \tau_i$.

The trajectory of the pseudoparticle is then integrated for a distance λ' , while accounting for blockage or absorption by physical obscurations. If the pseudoparticle leaves the plasma, its weighting and equivalent flux are binned as a function of frequency and location. These quantities summed over all pseudoparticles emitted by a particular transition will provide the spectrum and photon flux leaving the plasma. If the photon remains in the plasma after traversing a distance λ' to location \vec{r}' an absorption may have occurred depending on the mean free path at \vec{r}' compared to the randomly selected λ' based on the minimum mean free path $\lambda_{im}(\nu)$. A random number ρ is selected. If $\rho \leq \lambda_{im}(\nu) / \lambda_i(\vec{r}', \nu)$, then an actual absorption occurred. If the inequality does not hold, then the absorption was null. In that case, another randomly selected mean free path is chosen and the photon's trajectory continues to be integrated in the same direction. As the pseudoparticle moves through the mesh, its trajectory and weighting are recorded and summed to provide a photon flux for transition i as a function of position, $\phi_i(\vec{r})$.

If an actual absorption occurs, then the particular absorption process that occurred, j , is determined from the process that satisfies

$$\lambda_i(\vec{r}, \nu) \sum_{k=1}^{j-1} N_k(\vec{r}) \sigma_k(\vec{r}, \nu) < \rho < \lambda_i(\vec{r}, \nu) \sum_{k=1}^j N_k(\vec{r}) \sigma_k(\vec{r}, \nu) \quad (9)$$

where both resonant and nonresonant absorption processes are included in the sums. If the absorption is nonresonant, then the pseudoparticle is removed from the simulation since that quantum of energy will not be directly re-emitted by the same transition. If the absorption is resonant, then another randomly chosen lifetime is computed, $\tau_i = -A_i^{-1} \ln(\rho)$, as the duration of time that this quanta of energy resides in the excited state. If $\tau_i > -\ln(\rho) f_{Qi}^{-1}$, then a quenching collision occurs before the absorbed quantum of energy could be re-emitted as a photon, and that quantum of energy is removed from the RTM. If the inequality does not hold, then the quantum of energy is re-emitted as a photon. At that point, we increment the running tally of the cumulative lifetime of the quanta of energy, $\tau_{Ci} = \tau_{Ci} + \tau_i + L/c$, where L is the length of the path from its previous emission to the absorption site. (In practice L/c is much smaller than τ_i .) The frequency of the re-emitted photon is selected in the following manner consisted with partial frequency redistribution.

If $\tau_i < -\ln(\rho) f_{Ni}^{-1}$, then the quantum of energy is emitted prior to a nonquenching, broadening, or velocity-changing collision occurring. In this case, energy conservation requires that the photon be remitted within the natural uncertainty of the frequency of the absorbed photon. The frequency of emission is randomly selected from a Lorentzian broadened line-shape function, $g_H(\nu)$, centered on the frequency of absorption having full width half maximum (FWHM) $\Delta\nu_{iH} = \frac{1}{2\pi}(A_i + A_l)$.

If $\tau_i \geq -\ln(\rho)f_{N_i}^{-1}$ then a nonquenching collision occurred prior to emission. If that collision is a velocity-changing collision, then the photon is emitted with a frequency randomly chosen from the Voigt profile $g_i(\vec{r}, \nu)$ to reflect the new Doppler-shifted frequency of emission. If the collision is a phase-changing collision, then the emission frequency is again chosen from a Lorentzian lineshape where the FWHM is $\Delta\nu_{iH}(\vec{r})$. Another randomly selected mean free path λ' is chosen based on the minimum mean free path of the new frequency $\lambda_{im}(\nu)$ and the photon is emitted in a random direction. The photon's trajectory is then integrated as described above. The process is continued until the pseudoparticle leaves the system by striking a surface or is absorbed by a gas-phase species. The model does not now allow reflection of photons from surfaces. However, this feature could be implemented by specifying a reflection probability and the nature of the reflection (specular or diffuse) and reinitializing the trajectory of the photon pseudoparticle back into the plasma upon striking a reflective surface.

The process just described has an intrinsic weakness in that very few particles are emitted in the wings of the lineshape function. These are precisely the photons that have a sufficiently long mean free path to escape the plasma and so the resulting photon fluxes leaving the plasma have poor statistics. An alternate method of initializing the photon pseudoparticles is to randomly but uniformly distribute the initial frequency of emission across the Voigt profile. In this case, the initial weighting of the pseudoparticle is given by $w_i(\vec{r}) = \frac{N_i(\vec{r})A_i\Delta V(\vec{r})}{n_i(\vec{r})}g_i(\vec{r}, \nu)$. The formerly described method is cleaner in that the weighting of the pseudoparticles is more uniform. However, it has the disadvantage of having to use a large number of particles to populate the wings of the lineshape function. The latter technique requires fewer pseudoparticles to properly represent the full lineshape function but results in the weightings of the particles having a large dynamic range.

The number of pseudoparticles emitted from each numerical mesh cell, $n_i(\vec{r})$, for each transition varies between the user-specified limits n_{\min} and n_{\max} depending on the relative density of the excited state at that location,

$$n_i(\vec{r}) = n_{\min} + (n_{\max} - n_{\min}) \frac{\log(N_i(\vec{r})) - \log(N_{i\min})}{\log(N_{i\max}) - \log(N_{i\min})} \quad (10)$$

where $N_{i\min}$ and $N_{i\max}$ are the minimum and maximum values of N_i in the numerical mesh. The RTM is executed during every iteration through the HPEM, which can number into the hundreds, and so a tradeoff is required between computational expediency and fully resolving the spectral features. Having made this tradeoff, typical values are $n_{\min} = 100$ and $n_{\max} = 1000$, which for numerical meshes which are on the order of 80×80 (in the plasma zone), results in about 3×10^6 pseudoparticles per transition every time the RTM is called. Given trapping factors of many hundreds, the number of absorptions and remissions per call to the RTM is on the order of 10^9 .

After the trajectories of all the pseudoparticles from a given transition are completed, the average lifetime of the

photon pseudoparticles in the plasma is calculated from the weighted sums of the τ_{Ci} . This weighted sum, normalized by the total weighting of the escaping photons, yields the effective radiative lifetime, τ_{ei} , of the resonant excited state producing photon i as observed from outside the plasma. The radiative trapping factor for the transition i is then $T_i = \tau_{ei}A_i$.

Photon pseudoparticles are emitted from all locations in the plasma having an excited-state population. A spatially average radiation trapping factor, T_i , is computed by

$$T_i = A_i \frac{\sum_k w_k \tau_{Ck}}{\sum_k w_k} \quad (11)$$

where the sum is over all of the photons pseudoparticles emitted for the particular transition. The radiative lifetime of the excited state in the FKM in the next iteration of the HPEM is then extended by the radiation trapping factor T_i . This is done on a plasma-wide basis which involves another tradeoff involving computational expediency. Since T_i is dominated by the density and temperature of the absorbing state and collision partners, which do not significantly vary for these conditions (in which the density of radiating states is large), this spatially averaged trapping factor is acceptably accurate. Two other methods have been investigated to feed back the results of the RTM to the FKM. The first is to maintain the natural lifetime of the upper state of the resonant transition and explicitly include absorption of the resonant transition in the FKM using the computed photon flux, $\phi_i(\vec{r})$. This technique provided essentially the same result as using the trapping factors but required many more pseudoparticles to reduce numerical noise. The second was to compute a spatially dependent T_i , which again did not significantly change the end result while requiring significantly more computing resources. The exception is when the spatial distribution of emitters changes, to be discussed below.

The RTM was validated by creating conditions in which broadening is dominated by either Doppler or Lorentzian processes in a long cylindrical geometry having uniform radiators. Volume-averaged radiation trapping values were computed and compared to analytic expressions for these conditions derived by Holstein [36]. Agreement with the Holstein radiation trapping values were within 20%.

In this paper, we discuss results for ICPs sustained in Ar, He/Ar, and Ar/Xe gas mixtures. The atomic model for Ar consists of eight levels: Ar, Ar(1s₅), Ar(1s₄), Ar(1s₃), Ar(1s₂), Ar(4p), Ar(4d), and Ar⁺. Ar(4p) is a lumped excited state that includes Ar(4p, 3d, 5s, and 5p). Ar(4d) is a lumped excited state that includes Ar(4d, 6s, and Rydberg states). The molecular states Ar₂^{*} and Ar₂⁺ were also included; however, their densities are 100–1000 times lower than their atomic counterparts. The reaction mechanism for Ar is given in table 1. The two resonance transitions Ar(1s₄) → Ar (104.8 nm), Ar(1s₂) → Ar (106.7 nm), and excimer emission from Ar₂^{*} at 121 nm are tracked in the RTM. The secondary emission coefficient for electrons on the substrate by ions is 0.15 and is 0.05 on other surfaces. For excited states, the secondary emission

Table 1. Reaction mechanism for Ar plasmas.

Species					
Ar	Ar(1s ₅)	Ar(1s ₄)	Ar(1s ₃)	Ar(1s ₂)	
Ar(4p)	Ar(4d)	Ar ⁺	Ar ₂ [*]	Ar ₂ ⁺	e
<i>hν</i> _{105nm}	<i>hν</i> _{107nm}	<i>hν</i> _{121nm}			
Reactions					
Process	Rate coefficient ^a		Reference	−Δ <i>H</i> (eV) ^a	
<i>Photoionization</i>					
<i>hν</i> _{105nm} + Ar(1s ₅) → Ar ⁺ + e	9.8 × 10 ^{−20} cm ²		[42] ^b		
<i>hν</i> _{105nm} + Ar(1s ₄) → Ar ⁺ + e	9.8 × 10 ^{−20} cm ²		[42] ^b		
<i>hν</i> _{105nm} + Ar(1s ₃) → Ar ⁺ + e	9.8 × 10 ^{−20} cm ²		[42] ^b		
<i>hν</i> _{105nm} + Ar(1s ₂) → Ar ⁺ + e	9.8 × 10 ^{−20} cm ²		[42] ^b		
<i>hν</i> _{105nm} + Ar(4p) → Ar ⁺ + e	9.3 × 10 ^{−20} cm ²		[42] ^b		
<i>hν</i> _{105nm} + Ar(4d) → Ar ⁺ + e	9.0 × 10 ^{−20} cm ²		[42] ^b		
<i>hν</i> _{107nm} + Ar(1s ₅) → Ar ⁺ + e	9.8 × 10 ^{−20} cm ²		[42] ^b		
<i>hν</i> _{107nm} + Ar(1s ₄) → Ar ⁺ + e	9.8 × 10 ^{−20} cm ²		[42] ^b		
<i>hν</i> _{107nm} + Ar(1s ₃) → Ar ⁺ + e	9.8 × 10 ^{−20} cm ²		[42] ^b		
<i>hν</i> _{107nm} + Ar(1s ₂) → Ar ⁺ + e	9.8 × 10 ^{−20} cm ²		[42] ^b		
<i>hν</i> _{107nm} + Ar(4p) → Ar ⁺ + e	9.3 × 10 ^{−20} cm ²		[42] ^b		
<i>hν</i> _{107nm} + Ar(4d) → Ar ⁺ + e	9.0 × 10 ^{−20} cm ²		[42] ^b		
<i>hν</i> _{121nm} + Ar(1s ₅) → Ar ⁺ + e	9.8 × 10 ^{−20} cm ²		[42] ^b		
<i>hν</i> _{121nm} + Ar(1s ₄) → Ar ⁺ + e	9.8 × 10 ^{−20} cm ²		[42] ^b		
<i>hν</i> _{121nm} + Ar(1s ₃) → Ar ⁺ + e	9.8 × 10 ^{−20} cm ²		[42] ^b		
<i>hν</i> _{121nm} + Ar(1s ₂) → Ar ⁺ + e	9.8 × 10 ^{−20} cm ²		[42] ^b		
<i>hν</i> _{121nm} + Ar(4p) → Ar ⁺ + e	9.3 × 10 ^{−20} cm ²		[42] ^b		
<i>hν</i> _{121nm} + Ar(4d) → Ar ⁺ + e	9.0 × 10 ^{−20} cm ²		[42] ^b		
<i>Radiative transitions</i>					
Ar(1s ₄) ↔ Ar	1.2 × 10 ⁸ s ^{−1}		[43] ^c		
Ar(1s ₂) ↔ Ar	5.1 × 10 ⁸ s ^{−1}		[43] ^c		
Ar(4p) → Ar(1s ₅)	1.6 × 10 ⁷ s ^{−1}		[44]		
Ar(4p) → Ar(1s ₄)	9.3 × 10 ⁶ s ^{−1}		[44]		
Ar(4p) → Ar(1s ₃)	3.0 × 10 ⁷ s ^{−1}		[44]		
Ar(4p) → Ar(1s ₂)	8.5 × 10 ⁶ s ^{−1}		[44]		
Ar(4d) → Ar(1s ₅)	2.0 × 10 ⁵ s ^{−1}		[44]		
Ar(4d) → Ar(1s ₄)	2.0 × 10 ⁵ s ^{−1}		[44]		
Ar(4d) → Ar(1s ₃)	2.0 × 10 ⁵ s ^{−1}		[44]		
Ar(4d) → Ar(1s ₂)	2.0 × 10 ⁵ s ^{−1}		[44]		
Ar(4d) → Ar(4p)	1.6 × 10 ⁷ s ^{−1}		[44]		
Ar ₂ [*] → Ar + Ar	6.0 × 10 ⁷ s ^{−1}		[45]	1.08	
<i>Electron impact processes</i>					
e + Ar → Ar + e	d		[46]	j	
e + Ar ↔ Ar(1s ₅) + e	d		[47] ^d		
e + Ar ↔ Ar(1s ₄) + e	d		[47] ^d		
e + Ar ↔ Ar(1s ₃) + e	d		[47] ^d		
e + Ar ↔ Ar(1s ₂) + e	d		[47] ^d		
e + Ar ↔ Ar(4p) + e	d		[47] ^{d,e}		
e + Ar ↔ Ar(4d) + e	d		[47] ^{d,f}		
e + Ar → Ar ⁺ + e + e	d		[48]		
e + Ar(1s ₅) ↔ Ar(1s ₄) + e	d		[49] ^d		
e + Ar(1s ₅) ↔ Ar(1s ₃) + e	d		[49] ^d		
e + Ar(1s ₅) ↔ Ar(1s ₂) + e	d		[49] ^d		

(Continued)

Table 1. (Continued)

Reactions			
Process	Rate coefficient ^a	Reference	$-\Delta H$ (eV) ^a
$e + \text{Ar}(1s_5) \leftrightarrow \text{Ar}(4p) + e$	d	[50] ^{d,g}	
$e + \text{Ar}(1s_5) \leftrightarrow \text{Ar}(4d) + e$	d	[50] ^{d,g}	
$e + \text{Ar}(1s_5) \rightarrow \text{Ar}^+ + e + e$	d	[51]	
$e + \text{Ar}(1s_4) \leftrightarrow \text{Ar}(1s_3) + e$	d	[49] ^d	
$e + \text{Ar}(1s_4) \leftrightarrow \text{Ar}(1s_2) + e$	d	[49] ^d	
$e + \text{Ar}(1s_4) \leftrightarrow \text{Ar}(4p) + e$	d	[50] ^{d,g}	
$e + \text{Ar}(1s_4) \leftrightarrow \text{Ar}(4d) + e$	d	[50] ^{d,g}	
$e + \text{Ar}(1s_4) \rightarrow \text{Ar}^+ + e + e$	d	[51]	
$e + \text{Ar}(1s_3) \leftrightarrow \text{Ar}(1s_2) + e$	d	[49] ^d	
$e + \text{Ar}(1s_3) \leftrightarrow \text{Ar}(4p) + e$	d	[50] ^{d,g}	
$e + \text{Ar}(1s_3) \leftrightarrow \text{Ar}(4d) + e$	d	[50] ^{d,g}	
$e + \text{Ar}(1s_3) \rightarrow \text{Ar}^+ + e + e$	d	[51]	
$e + \text{Ar}(1s_2) \leftrightarrow \text{Ar}(4p) + e$	d	[50] ^{d,g}	
$e + \text{Ar}(1s_2) \leftrightarrow \text{Ar}(4d) + e$	d	[50] ^{d,g}	
$e + \text{Ar}(1s_2) \rightarrow \text{Ar}^+ + e + e$	d	[51]	
$e + \text{Ar}(4p) \leftrightarrow \text{Ar}(4d) + e$	d	[50] ^{d,g}	
$e + \text{Ar}(4p) \rightarrow \text{Ar}^+ + e + e$	d	[51]	
$e + \text{Ar}(4d) \rightarrow \text{Ar}^+ + e + e$	d	[51]	
$e + e + \text{Ar}^+ \rightarrow \text{Ar}(1s_5) + e$	$5.0 \times 10^{-27} T_e^{9/2} \text{cm}^6 \text{s}^{-1}$	[52]	
$e + \text{Ar}^+ \rightarrow \text{Ar}(1s_5)$	$4.0 \times 10^{-13} T_e^{-1/2}$	[52]	
$\text{Ar}(1s_5) + \text{Ar} \rightarrow \text{Ar}(1s_4) + \text{Ar}$	$1.5 \times 10^{-15} T_n^{1/2} \exp(-881/T_g)$	[44] ^m	-0.076
$\text{Ar}(1s_4) + \text{Ar} \rightarrow \text{Ar}(1s_5) + \text{Ar}$	$2.5 \times 10^{-15} T_n^{1/2}$	[44]	0.076
$\text{Ar}(1s_5) + \text{Ar} \rightarrow \text{Ar}(1s_3) + \text{Ar}$	$0.5 \times 10^{-15} T_n^{1/2} \exp(-2029/T_g)$	[44] ^m	-0.175
$\text{Ar}(1s_3) + \text{Ar} \rightarrow \text{Ar}(1s_5) + \text{Ar}$	$2.5 \times 10^{-15} T_n^{1/2}$	[44]	0.175
$\text{Ar}(1s_5) + \text{Ar} \rightarrow \text{Ar}(1s_2) + \text{Ar}$	$1.5 \times 10^{-15} T_n^{1/2} \exp(-3246/T_g)$	[44] ^m	-0.280
$\text{Ar}(1s_2) + \text{Ar} \rightarrow \text{Ar}(1s_5) + \text{Ar}$	$2.5 \times 10^{-15} T_n^{1/2}$	[44]	0.280
$\text{Ar}(1s_4) + \text{Ar} \rightarrow \text{Ar}(1s_3) + \text{Ar}$	$0.83 \times 10^{-15} T_n^{1/2} \exp(-1148/T_g)$	[44] ^m	-0.099
$\text{Ar}(1s_3) + \text{Ar} \rightarrow \text{Ar}(1s_4) + \text{Ar}$	$2.5 \times 10^{-15} T_n^{1/2}$	[44]	0.099
$\text{Ar}(1s_4) + \text{Ar} \rightarrow \text{Ar}(1s_2) + \text{Ar}$	$2.5 \times 10^{-15} T_n^{1/2} \exp(-2365/T_g)$	[44] ^m	-0.204
$\text{Ar}(1s_2) + \text{Ar} \rightarrow \text{Ar}(1s_4) + \text{Ar}$	$2.5 \times 10^{-15} T_n^{1/2}$	[44]	0.204
$\text{Ar}(1s_3) + \text{Ar} \rightarrow \text{Ar}(1s_2) + \text{Ar}$	$7.5 \times 10^{-15} T_n^{1/2} \exp(-1217/T_g)$	[44] ^m	-0.105
$\text{Ar}(1s_2) + \text{Ar} \rightarrow \text{Ar}(1s_3) + \text{Ar}$	$2.5 \times 10^{-15} T_n^{1/2}$	[44]	0.105
$\text{Ar}^* + \text{Ar}^* \rightarrow \text{Ar}^+ + \text{Ar} + e$	$1.2 \times 10^{-9} T_n^{1/2}$	[44] ^{h,i}	
$\text{Ar}^+ + \text{Ar} \rightarrow \text{Ar}^+ + \text{Ar}$	$5.66 \times 10^{-10} T_n^{1/2}$	[53]	k
$\text{Ar}(1s_5) + \text{Ar} + \text{Ar} \rightarrow \text{Ar}_2^* + \text{Ar}$	$1.14 \times 10^{-32} T_n^{-1}$	[45]	0.72
$\text{Ar}(1s_4) + \text{Ar} + \text{Ar} \rightarrow \text{Ar}_2^* + \text{Ar}$	$1.14 \times 10^{-32} T_n^{-1}$	[45]	0.79
$\text{Ar}(1s_3) + \text{Ar} + \text{Ar} \rightarrow \text{Ar}_2^* + \text{Ar}$	$1.14 \times 10^{-32} T_n^{-1}$	[45]	0.89
$\text{Ar}(1s_2) + \text{Ar} + \text{Ar} \rightarrow \text{Ar}_2^* + \text{Ar}$	$1.14 \times 10^{-32} T_n^{-1}$	[45]	1.00
$\text{Ar}(4p) + \text{Ar} + \text{Ar} \rightarrow \text{Ar}_2^* + \text{Ar}$	$1.14 \times 10^{-32} T_n^{-1}$	[45]	2.08
$\text{Ar}(4d) + \text{Ar} + \text{Ar} \rightarrow \text{Ar}_2^* + \text{Ar}$	$1.14 \times 10^{-32} T_n^{-1}$	[45]	3.88
$\text{Ar}^* + \text{Ar}^* \rightarrow \text{Ar}_2^+ + e$	$5.7 \times 10^{-10} T_n^{1/2}$	[54] ^{h,i}	
$\text{Ar}(4d) + \text{Ar} \rightarrow \text{Ar}_2^+ + e$	$2.0 \times 10^{-9} T_n^{1/2}$	[55]	0.33

(Continued)

Table 1. (Continued)

Reactions			
Process	Rate coefficient ^a	Reference	$-\Delta H$ (eV) ^a
$\text{Ar}^+ + \text{Ar} + \text{Ar} \rightarrow \text{Ar}_2^+ + \text{Ar}$	$2.5 \times 10^{-31} T_n^{-1}$	[56]	1.35
$\text{Ar}_2^* + \text{Ar}_2^* \rightarrow \text{Ar}_2^+ + \text{Ar} + \text{Ar} + e$	$5.0 \times 10^{-10} T_n^{1/2}$	[45]	
$e + \text{Ar}_2^+ \rightarrow \text{Ar}(1s_5) + \text{Ar}$	$2.69 \times 10^{-8} T_e^{-0.67}$	[57] ^l	2.89
$e + \text{Ar}_2^+ \rightarrow \text{Ar} + \text{Ar}$	$2.69 \times 10^{-8} T_e^{-0.67}$	[57] ^l	14.44
$e + \text{Ar}_2^* \rightarrow \text{Ar}_2^+ + e + e$	$9.0 \times 10^{-8} T_e^{-0.7} \exp(-3.66/T_e)$	[45]	
$e + \text{Ar}_2^* \rightarrow \text{Ar} + \text{Ar} + e$	1.0×10^{-7}	[45]	

^a Rate coefficients have units of $\text{cm}^3 \text{s}^{-1}$ unless noted. T_e is electron temperature (eV). T_g is gas temperature (K), T_n is normalized gas temperature ($T_g/300\text{K}$). $-\Delta H$ is the contribution to gas heating (eV).

^b Photoionization cross sections for higher levels were scaled from that of the metastable state based on the energies of the ejected electron.

^c Rate shown is for emission. Absorption is addressed using a radiation trapping factor. (See text.)

^d Cross section is for forward reaction. Reverse cross section obtained by detailed balance.

^e Lumped state has excitation cross sections to Ar(4p, 3d, 5s, 5p).

^f Lumped state has excitation cross sections to Ar(4d, 6s, Rydberg).

^g Sum of electron impact excitation to optically allowed and forbidden states comprising the lumped Ar(4p) or Ar(4d).

^h Ar* represents any excited atomic state of Ar.

ⁱ The same Penning-ionization rate coefficient was used for all pairings of excited states of Ar.

^j The rate of heating by elastic collisions is $k_m(3/2)k_B(2m_e/M)(T_e - T_g) \text{ eV cm}^3 \text{ s}^{-1}$, for elastic rate coefficient k_m , electron mass m_e , neutral mass M , and Boltzmann's constant k_B .

^k The rate of gas heating of the neutral particles by charge exchange is $k_{ce}(3/2)k_B(T_{ion} - T_g) \text{ eV cm}^3 \text{ s}^{-1}$, for charge exchange rate coefficient k_{ce} and ion temperature T_{ion} .

^l Equal branching assumed.

^m Rate coefficient obtained by detailed balancing.

probability was 0.03 on the substrate and 0.01 on other surfaces. For VUV photons, the secondary emission probability was 0.01 on all surfaces.

To investigate tuning of the VUV spectra emitted by low-pressure ICPs, two additional gas mixtures were considered: Ar/Xe mixtures that will produce VUV from Xe with longer wavelengths than from Ar, and Ar/He mixtures that will produce VUV from He with shorter wavelengths than from Ar. The reaction mechanism for Ar/Xe mixtures has the following additional species: Xe, Xe(1s₅), Xe(1s₄), Xe(1s₃), Xe(1s₂), Xe(6p), Xe(5d), Xe(7s), Xe(7p), Xe⁺, Xe₂^{*}, and Xe₂⁺. The Xe(7p) state is an effective lumped state comprising Xe(7p, 6d, 8s, 7d, 9s, 9d, 10s, 10d, and higher Rydberg states). The two resonance transitions Xe(1s₄) → Xe (129.76 nm) and Xe(1s₂) → Xe (147.1 nm), and excimer emission from Xe₂^{*} at 174 nm are tracked in the RTM. The additional reactions for Ar/Xe mixtures are listed in table 2. The reaction mechanism for Ar/He mixtures has the following additional species: He, He(2³S), He(2¹S), He(2³P), He(2¹P), He(3s), He(3p), and He⁺. He(3p) is a lumped state of all higher states. Emission from He(2¹P) → He (59.1 nm) is considered in RTM. The additional reactions for Ar/He mixtures are listed in table 3.

3. Plasma dynamics in ICPs

A schematic of the reactor used in this investigation is shown in figure 1. The simulation is cylindrically symmetric and 2D. The intent of this study was not to model a specific configuration but rather to discuss more general properties of VUV emission from ICPs, and so we have chosen a simple geometry. The reactor has a diameter of 22.5 cm and substrate to window height of 12 cm. Gas is fed into the reactor through an

annular nozzle at the top and exhausted by an annular pumpport at the bottom. VUV and ion fluxes will be discussed averaged over the substrate. The plasma is sustained by inductively coupled electromagnetic fields produced by a three-turn coil powered at 10 MHz. We will first discuss VUV emission from the base case plasma sustained in Ar at 20 mTorr and a cw power of 150 W.

The electron density, n_e , temperature, T_e , and densities of the metastable Ar(1s₅) and radiative Ar(1s₄) states are shown in figure 2. The VUV within the plasma for the 106.7 and 104.8 nm transitions are also shown. In the steady state, the diffusive plasma has a peak electron density of $2.8 \times 10^{11} \text{ cm}^{-3}$. The metastable Ar(1s₅) and radiative Ar(1s₄) states have peak densities of $3.2 \times 10^{11} \text{ cm}^{-3}$ and $9.8 \times 10^{10} \text{ cm}^{-3}$ respectively. T_e peaks beneath the coils at up to 3.5 eV. The excited state densities are skewed towards the location of maximum power deposition under the coils. The lifetimes, either radiative or by electron collision quenching, of the excited states are shorter than the lifetime of ions due to loss by diffusion. The distribution of excited states therefore more closely reflect their sources by electron impact, which are maximum under the coils, compared to the spatial distribution of ions. The density of Ar under the inlet is $5.2 \times 10^{14} \text{ cm}^{-3}$, whereas near the axis of the reactor beneath the coil the Ar density is $3.4 \times 10^{14} \text{ cm}^{-3}$. (The gas near the axis of the reactor beneath the coil is additionally rarefied by gas heating producing a temperature of 571 K).

The VUV fluxes have maximum values of $10^{17} \text{ cm}^{-2} \text{ s}^{-1}$ for the 104.8 nm transition and $10^{18} \text{ cm}^{-2} \text{ s}^{-1}$ for the 106.7 nm transition. The larger VUV fluxes for the transition originating from the lower Ar(1s₄) resonant state are in large part a consequence of the collisional coupling of the heavily populated

Table 2. Reaction mechanism for Ar/Xe plasmas.

Species						
Ar	Ar(1s ₅)	Ar(1s ₄)	Ar(1s ₃)	Ar(1s ₂)	Ar(4p)	
Ar(4d)	Ar ⁺	Ar ₂ [*]	Ar ₂ [‡]			
Xe	Xe(1s ₅)	Xe(1s ₄)	Xe(1s ₃)	Xe(1s ₂)	Xe(6p)	
Xe(5d)	Xe(7s)	Xe(3p)	Xe ₂ [*]	Xe ⁺	Xe ₂ [‡]	e
<i>hν</i> _{105nm}	<i>hν</i> _{107nm}	<i>hν</i> _{121nm}	<i>hν</i> _{130nm}	<i>hν</i> _{147nm}	<i>hν</i> _{172nm}	
Reactions (Note: Reactions involving only Ar species are listed in table 1.)						
Process	Rate coefficient ^a			Reference	−Δ <i>H</i> (eV) ^a	
<i>Photoionization</i>						
<i>hν</i> _{130nm} + Xe(1s ₅) → Xe ⁺ + e	3.53 × 10 ^{−20} cm ²			[42] ^b		
<i>hν</i> _{130nm} + Xe(1s ₄) → Xe ⁺ + e	3.54 × 10 ^{−20} cm ²			[42] ^b		
<i>hν</i> _{130nm} + Xe(1s ₃) → Xe ⁺ + e	3.56 × 10 ^{−20} cm ²			[42] ^b		
<i>hν</i> _{130nm} + Xe(1s ₂) → Xe ⁺ + e	3.55 × 10 ^{−20} cm ²			[42] ^b		
<i>hν</i> _{130nm} + Xe(6p) → Xe ⁺ + e	3.55 × 10 ^{−20} cm ²			[42] ^b		
<i>hν</i> _{130nm} + Xe(5d) → Xe ⁺ + e	3.53 × 10 ^{−20} cm ²			[42] ^b		
<i>hν</i> _{130nm} + Xe(7s) → Xe ⁺ + e	3.48 × 10 ^{−20} cm ²			[42] ^b		
<i>hν</i> _{130nm} + Xe(3p) → Xe ⁺ + e	3.44 × 10 ^{−20} cm ²			[42] ^b		
<i>hν</i> _{147nm} + Xe(1s ₅) → Xe ⁺ + e	3.35 × 10 ^{−20} cm ²			[42] ^b		
<i>hν</i> _{147nm} + Xe(1s ₄) → Xe ⁺ + e	3.37 × 10 ^{−20} cm ²			[42] ^b		
<i>hν</i> _{147nm} + Xe(1s ₃) → Xe ⁺ + e	3.53 × 10 ^{−20} cm ²			[42] ^b		
<i>hν</i> _{147nm} + Xe(1s ₂) → Xe ⁺ + e	3.54 × 10 ^{−20} cm ²			[42] ^b		
<i>hν</i> _{147nm} + Xe(6p) → Xe ⁺ + e	3.54 × 10 ^{−20} cm ²			[42] ^b		
<i>hν</i> _{147nm} + Xe(5d) → Xe ⁺ + e	3.55 × 10 ^{−20} cm ²			[42] ^b		
<i>hν</i> _{147nm} + Xe(7s) → Xe ⁺ + e	3.56 × 10 ^{−20} cm ²			[42] ^b		
<i>hν</i> _{147nm} + Xe(3p) → Xe ⁺ + e	3.53 × 10 ^{−20} cm ²			[42] ^b		
<i>hν</i> _{172nm} + Xe(1s ₅) → Xe ⁺ + e	2.61 × 10 ^{−20} cm ²			[42] ^b		
<i>hν</i> _{172nm} + Xe(1s ₄) → Xe ⁺ + e	2.72 × 10 ^{−20} cm ²			[42] ^b		
<i>hν</i> _{172nm} + Xe(1s ₃) → Xe ⁺ + e	3.33 × 10 ^{−20} cm ²			[42] ^b		
<i>hν</i> _{172nm} + Xe(1s ₂) → Xe ⁺ + e	3.35 × 10 ^{−20} cm ²			[42] ^b		
<i>hν</i> _{172nm} + Xe(6p) → Xe ⁺ + e	3.35 × 10 ^{−20} cm ²			[42] ^b		
<i>hν</i> _{172nm} + Xe(5d) → Xe ⁺ + e	3.42 × 10 ^{−20} cm ²			[42] ^b		
<i>hν</i> _{172nm} + Xe(7s) → Xe ⁺ + e	3.53 × 10 ^{−20} cm ²			[42] ^b		
<i>hν</i> _{172nm} + Xe(3p) → Xe ⁺ + e	3.54 × 10 ^{−20} cm ²			[42] ^b		
<i>hν</i> _{107nm} + Xe(1s ₅) → Xe ⁺ + e	3.47 × 10 ^{−20} cm ²			[42] ^b		
<i>hν</i> _{107nm} + Xe(1s ₄) → Xe ⁺ + e	3.47 × 10 ^{−20} cm ²			[42] ^b		
<i>hν</i> _{107nm} + Xe(1s ₃) → Xe ⁺ + e	3.31 × 10 ^{−20} cm ²			[42] ^b		
<i>hν</i> _{107nm} + Xe(1s ₂) → Xe ⁺ + e	3.29 × 10 ^{−20} cm ²			[42] ^b		
<i>hν</i> _{107nm} + Xe(6p) → Xe ⁺ + e	3.29 × 10 ^{−20} cm ²			[42] ^b		
<i>hν</i> _{107nm} + Xe(5d) → Xe ⁺ + e	3.24 × 10 ^{−20} cm ²			[42] ^b		
<i>hν</i> _{107nm} + Xe(7s) → Xe ⁺ + e	3.14 × 10 ^{−20} cm ²			[42] ^b		
<i>hν</i> _{107nm} + Xe(3p) → Xe ⁺ + e	3.08 × 10 ^{−20} cm ²			[42] ^b		
<i>hν</i> _{105nm} + Xe(1s ₅) → Xe ⁺ + e	3.47 × 10 ^{−20} cm ²			[42] ^b		
<i>hν</i> _{105nm} + Xe(1s ₄) → Xe ⁺ + e	3.47 × 10 ^{−20} cm ²			[42] ^b		
<i>hν</i> _{105nm} + Xe(1s ₃) → Xe ⁺ + e	3.31 × 10 ^{−20} cm ²			[42] ^b		
<i>hν</i> _{105nm} + Xe(1s ₂) → Xe ⁺ + e	3.29 × 10 ^{−20} cm ²			[42] ^b		
<i>hν</i> _{105nm} + Xe6SP → Xe ⁺ + e	3.29 × 10 ^{−20} cm ²			[42] ^b		
<i>hν</i> _{105nm} + Xe(5d) → Xe ⁺ + e	3.24 × 10 ^{−20} cm ²			[42] ^b		
<i>hν</i> _{105nm} + Xe(7s) → Xe ⁺ + e	3.14 × 10 ^{−20} cm ²			[42] ^b		
<i>hν</i> _{105nm} + Xe(3p) → Xe ⁺ + e	3.08 × 10 ^{−20} cm ²			[42] ^b		
<i>hν</i> _{130nm} + Ar(1s ₅) → Ar ⁺ + e	1.01 × 10 ^{−19} cm ²			[42] ^b		
<i>hν</i> _{130nm} + Ar(1s ₄) → Ar ⁺ + e	1.01 × 10 ^{−19} cm ²			[42] ^b		
<i>hν</i> _{130nm} + Ar(1s ₃) → Ar ⁺ + e	1.01 × 10 ^{−19} cm ²			[42] ^b		
<i>hν</i> _{130nm} + Ar(1s ₂) → Ar ⁺ + e	1.01 × 10 ^{−19} cm ²			[42] ^b		

(Continued)

Table 2. (Continued)

Reactions (Note: Reactions involving only Ar species are listed in table 1.)			
Process	Rate coefficient ^a	Reference	$-\Delta H$ (eV) ^a
$h\nu_{130\text{nm}} + \text{Ar}(4p) \rightarrow \text{Ar}^+ + e$	$9.92 \times 10^{-20} \text{cm}^2$	[42] ^b	
$h\nu_{130\text{nm}} + \text{Ar}(4d) \rightarrow \text{Ar}^+ + e$	$9.61 \times 10^{-20} \text{cm}^2$	[42] ^b	
$h\nu_{147\text{nm}} + \text{Ar}(1s_5) \rightarrow \text{Ar}^+ + e$	$9.61 \times 10^{-20} \text{cm}^2$	[42] ^b	
$h\nu_{147\text{nm}} + \text{Ar}(1s_4) \rightarrow \text{Ar}^+ + e$	$9.72 \times 10^{-20} \text{cm}^2$	[42] ^b	
$h\nu_{147\text{nm}} + \text{Ar}(1s_3) \rightarrow \text{Ar}^+ + e$	$9.78 \times 10^{-20} \text{cm}^2$	[42] ^b	
$h\nu_{147\text{nm}} + \text{Ar}(1s_2) \rightarrow \text{Ar}^+ + e$	$9.82 \times 10^{-20} \text{cm}^2$	[42] ^b	
$h\nu_{147\text{nm}} + \text{Ar}(4p) \rightarrow \text{Ar}^+ + e$	$1.01 \times 10^{-19} \text{cm}^2$	[42] ^b	
$h\nu_{147\text{nm}} + \text{Ar}(4d) \rightarrow \text{Ar}^+ + e$	$9.97 \times 10^{-20} \text{cm}^2$	[42] ^b	
$h\nu_{172\text{nm}} + \text{Ar}(1s_5) \rightarrow \text{Ar}^+ + e$	$7.81 \times 10^{-20} \text{cm}^2$	[42] ^b	
$h\nu_{172\text{nm}} + \text{Ar}(1s_4) \rightarrow \text{Ar}^+ + e$	$7.91 \times 10^{-20} \text{cm}^2$	[42] ^b	
$h\nu_{172\text{nm}} + \text{Ar}(1s_3) \rightarrow \text{Ar}^+ + e$	$8.06 \times 10^{-20} \text{cm}^2$	[42] ^b	
$h\nu_{172\text{nm}} + \text{Ar}(1s_2) \rightarrow \text{Ar}^+ + e$	$8.22 \times 10^{-20} \text{cm}^2$	[42] ^b	
$h\nu_{172\text{nm}} + \text{Ar}(4p) \rightarrow \text{Ar}^+ + e$	$9.78 \times 10^{-20} \text{cm}^2$	[42] ^b	
$h\nu_{172\text{nm}} + \text{Ar}(4d) \rightarrow \text{Ar}^+ + e$	$1.01 \times 10^{-19} \text{cm}^2$	[42] ^b	
<i>Radiative transitions</i>			
$\text{Xe}(1s_4) \leftrightarrow \text{Xe}$	$2.81 \times 10^8 \text{s}^{-1}$	[58] ^c	
$\text{Xe}(1s_2) \leftrightarrow \text{Xe}$	$2.46 \times 10^8 \text{s}^{-1}$	[58] ^c	
$\text{Xe}(3p) \rightarrow \text{Xe}(7s)$	$1.0 \times 10^6 \text{s}^{-1}$	[58] ^h	
$\text{Xe}(3p) \rightarrow \text{Xe}(5d)$	$1.0 \times 10^6 \text{s}^{-1}$	[58] ^h	
$\text{Xe}(3p) \rightarrow \text{Xe}(1s_2)$	$2.9 \times 10^6 \text{s}^{-1}$	[59]	
$\text{Xe}(3p) \rightarrow \text{Xe}(1s_3)$	$2.9 \times 10^6 \text{s}^{-1}$	[59]	
$\text{Xe}(3p) \rightarrow \text{Xe}(1s_4)$	$4.64 \times 10^6 \text{s}^{-1}$	[59]	
$\text{Xe}(3p) \rightarrow \text{Xe}(1s_5)$	$4.64 \times 10^6 \text{s}^{-1}$	[59]	
$\text{Xe}(7s) \rightarrow \text{Xe}(6p)$	$2.0 \times 10^6 \text{s}^{-1}$	[59] ^h	
$\text{Xe}(5d) \rightarrow \text{Xe}(6p)$	$2.0 \times 10^6 \text{s}^{-1}$	[59]	
$\text{Xe}(5d) \rightarrow \text{Xe}(1s_4)$	$5.0 \times 10^5 \text{s}^{-1}$	[59]	
$\text{Xe}(5d) \rightarrow \text{Xe}(1s_5)$	$5.0 \times 10^5 \text{s}^{-1}$	[59]	
$\text{Xe}(6p) \rightarrow \text{Xe}(1s_4)$	$5.0 \times 10^5 \text{s}^{-1}$	[59]	
$\text{Xe}(6p) \rightarrow \text{Xe}(1s_5)$	$5.0 \times 10^5 \text{s}^{-1}$	[59]	
$\text{Xe}_2^* \rightarrow \text{Xe} + \text{Xe}$	$6.0 \times 10^7 \text{s}^{-1}$	[60]	1.08
<i>Electron impact processes</i>			
$e + \text{Xe} \rightarrow +e$		[46]	^e
$e + \text{Xe} \leftrightarrow \text{Xe}(1s_5) + e$	d	[61]	
$e + \text{Xe} \leftrightarrow \text{Xe}(1s_4) + e$	d	[61]	
$e + \text{Xe} \leftrightarrow \text{Xe}(1s_2) + e$	d	[61]	
$e + \text{Xe} \leftrightarrow \text{Xe}(1s_3) + e$	d	[61]	
$e + \text{Xe} \leftrightarrow \text{Xe}(6p) + e$	d	[61]	
$e + \text{Xe} \leftrightarrow \text{Xe}(5d) + e$	d	[61]	
$e + \text{Xe} \leftrightarrow \text{Xe}(7s) + e$	d	[61]	
$e + \text{Xe} \leftrightarrow \text{Xe}(3p) + e$	d	[61]	
$e + \text{Xe} \rightarrow \text{Xe}^+ + e + e$		[61]	
$e + \text{Xe}(1s_5) \leftrightarrow \text{Xe}(1s_4) + e$	d	[48]	
$e + \text{Xe}(1s_5) \leftrightarrow \text{Xe}(1s_2) + e$	d	[48]	
$e + \text{Xe}(1s_5) \leftrightarrow \text{Xe}(1s_3) + e$	d	[48]	
$e + \text{Xe}(1s_5) \leftrightarrow \text{Xe}(6p) + e$	d	[48]	
$e + \text{Xe}(1s_5) \leftrightarrow \text{Xe}(5d) + e$	d	[48]	
$e + \text{Xe}(1s_5) \leftrightarrow \text{Xe}(7s) + e$	d	[48]	
$e + \text{Xe}(1s_5) \leftrightarrow \text{Xe}(3p) + e$	d	[48]	
$e + \text{Xe}(1s_5) \rightarrow \text{Xe}^+ + e + e$		[51]	
$e + \text{Xe}(1s_4) \leftrightarrow \text{Xe}(1s_2) + e$	d	[48]	
$e + \text{Xe}(1s_4) \leftrightarrow \text{Xe}(1s_3) + e$	d	[48]	
$e + \text{Xe}(1s_4) \leftrightarrow \text{Xe}(6p) + e$	d	[48]	

(Continued)

Table 2. (Continued)

Reactions (Note: Reactions involving only Ar species are listed in table 1.)			
Process	Rate coefficient ^a	Reference	$-\Delta H$ (eV) ^a
$e + Xe(1s_4) \leftrightarrow Xe(5d) + e$	d	[48]	
$e + Xe(1s_4) \leftrightarrow Xe(7s) + e$	d	[48]	
$e + Xe(1s_4) \leftrightarrow Xe(3p) + e$	d	[48]	
$e + Xe(1s_4) \rightarrow Xe^+ + e + e$		[51]	
$e + Xe(1s_3) \leftrightarrow Xe(1s_2) + e$	d	[48]	
$e + Xe(1s_3) \leftrightarrow Xe(6p) + e$	d	[48]	
$e + Xe(1s_3) \leftrightarrow Xe(5d) + e$	d	[48]	
$e + Xe(1s_3) \leftrightarrow Xe(7s) + e$	d	[48]	
$e + Xe(1s_3) \leftrightarrow Xe(3p) + e$	d	[48]	
$e + Xe(1s_3) \rightarrow Xe^+ + e + e$		[51]	
$e + Xe(1s_2) \leftrightarrow Xe(6p) + e$	d	[48]	
$e + Xe(1s_2) \leftrightarrow Xe(5d) + e$	d	[48]	
$e + Xe(1s_2) \leftrightarrow Xe(7s) + e$	d	[48]	
$e + Xe(1s_2) \leftrightarrow Xe(3p) + e$	d	[48]	
$e + Xe(1s_2) \rightarrow Xe^+ + e + e$		[51]	
$e + Xe(6p) \leftrightarrow Xe(5d) + e$	d	[48]	
$e + Xe(6p) \leftrightarrow Xe(7s) + e$	d	[48]	
$e + Xe(6p) \leftrightarrow Xe(3p) + e$	d	[48]	
$e + Xe(6p) \rightarrow Xe^+ + e + e$		[51]	
$e + Xe(5d) \leftrightarrow Xe(7s) + e$	d	[48]	
$e + Xe(5d) \leftrightarrow Xe(3p) + e$	d	[48]	
$e + Xe(5d) \rightarrow Xe^+ + e + e$		[51]	
$e + Xe(7s) \leftrightarrow Xe(3p) + e$	d	[48]	
$e + Xe(7s) \rightarrow Xe^+ + e + e$		[51]	
$e + Xe(3p) \rightarrow Xe^+ + e + e$		[51]	
$e + e + Xe^+ \rightarrow Xe(1s_5) + e$	$5.0 \times 10^{-27} T_e^{-9/2}$	[52]	
$e + Xe^+ \rightarrow Xe$	$4.0 \times 10^{-13} T_e^{-1/2}$	[52]	
$e + Xe_2^+ \rightarrow Xe(1s_5) + Xe$	$2.2 \times 10^{-7} T_e^{-1/2}$	[60]	2.7
$e + Xe_2^+ \rightarrow Xe + Xe + e$	1.0×10^{-9}	[72]	
<i>Heavy particle processes</i>			
$Xe^+ + Xe \rightarrow Xe^+ + Xe$	$3.78 \times 10^{-10} T_n^{-1/2}$	[69]	f
$Xe^+ + Xe + Xe \rightarrow Xe_2^+ + Xe$	$3.6 \times 10^{-31} T_n^{-1} cm^6 s^{-1}$	[60]	
$Xe_2^+ + Xe_2^+ \rightarrow Xe_2^+ + Xe + Xe + e$	3.5×10^{-10}	[60]	
$Xe(1s_5) + Xe \rightarrow Xe(1s_4) + Xe$	$0.6 \times 10^{-13} T_n^{-1/2} \exp(-1405/T_g)$	[73] ⁱ	- 0.12
$Xe(1s_4) + Xe \rightarrow Xe(1s_5) + Xe$	$1 \times 10^{-13} T_n^{-1/2}$	[73]	0.12
$Xe(1s_5) + Xe \rightarrow Xe(1s_3) + Xe$	$0.9 \times 10^{-12} T_n^{-1/2} \exp(-13,122/T_g)$	[73] ⁱ	- 1.13
$Xe(6p)M + Xe \rightarrow Xe(1s_5) + Xe$	$4.5 \times 10^{-12} T_n^{-1/2}$	[73]	1.13
$Xe(1s_5) + Xe \rightarrow Xe(1s_2) + Xe$	$2.7 \times 10^{-12} T_n^{-1/2} \exp(-14,544/T_g)$	[73] ⁱ	- 1.25
$Xe(1s_2) + Xe \rightarrow Xe(1s_5) + Xe$	$4.5 \times 10^{-12} T_n^{-1/2}$	[73]	1.25
$Xe(1s_3) + Xe \rightarrow Xe(1s_2) + Xe$	$7.5 \times 10^{-11} T_n^{-1/2} \exp(-1421/T_g)$	[73] ⁱ	- 0.12
$Xe(1s_2) + Xe \rightarrow Xe(1s_3) + Xe$	$2.5 \times 10^{-11} T_n^{-1/2}$	[73]	0.12
$Xe(1s_2) + Xe \rightarrow Xe(6p) + Xe$	$1.67 \times 10^{-10} T_n^{-1/2} \exp(-120/T_g)$	[73] ⁱ	- 0.01
$Xe(6p) + Xe \rightarrow Xe(1s_2) + Xe$	$1.0 \times 10^{-10} T_n^{-1/2}$	[73]	0.01
$Xe(1s_3) + Xe \rightarrow Xe(6p) + Xe$	$1.85 \times 10^{-10} T_n^{-1/2} \exp(-1620/T_g)$	[73] ⁱ	- 0.13
$Xe(6p) + Xe \rightarrow Xe(1s_3) + Xe$	$3.7 \times 10^{-11} T_n^{-1/2}$	[73]	0.13
$Xe(6p) + Xe \rightarrow Xe(3p) + Xe$	$4.2 \times 10^{-10} T_n^{-1/2} \exp(-15,300/T_g)$	[73] ⁱ	- 1.32
$Xe(3p) + Xe \rightarrow Xe(6p) + Xe$	$4.2 \times 10^{-10} T_n^{-1/2}$	[73]	1.32
$Xe(6p) + Xe \rightarrow Xe(5d) + Xe$	$9.5 \times 10^{-11} T_n^{-1/2} \exp(-3594/T_g)$	[59]	- 0.31
$Xe(5d) + Xe \rightarrow Xe(6p) + Xe$	$9.5 \times 10^{-11} T_n^{-1/2}$	[59]	0.31
$Xe^* + Xe^* \rightarrow Xe^+ + Xe + e$	$1.9 \times 10^{-10} T_n^{-1/2}$	[73] ^g	
$Xe^* + Xe + Xe \rightarrow Xe_2^+ + Xe$	$8.0 \times 10^{-32} T_n^{-3/4} cm^6 s^{-1}$	[73] ^g	

(Continued)

Table 2. (Continued)

Reactions (Note: Reactions involving only Ar species are listed in table 1.)			
Process	Rate coefficient ^a	Reference	$-\Delta H$ (eV) ^a
<i>Ar and Xe heavy particle processes</i>			
Ar(1s ₅) + Xe → Xe(3p) + Ar	$2.0 \times 10^{-10} T_n^{-1/2}$	est.	
Ar(1s ₄) + Xe → Xe(3p) + Ar	$2.0 \times 10^{-10} T_n^{-1/2}$	est.	
Ar(1s ₃) + Xe → Xe(3p) + Ar	$2.0 \times 10^{-10} T_n^{-1/2}$	est.	
Ar(1s ₂) + Xe → Xe(3p) + Ar	$2.0 \times 10^{-10} T_n^{-1/2}$	est.	
Ar(4p) + Xe → Xe ⁺ + Ar + e	$2.0 \times 10^{-10} T_n^{-1/2}$	est.	
Ar(4p) + Xe* → Xe ⁺ + Ar + e	$2.0 \times 10^{-10} T_n^{-1/2}$	est. ^g	
Ar(4d) + Xe → Xe ⁺ + Ar + e	$2.0 \times 10^{-10} T_n^{-1/2}$	est.	
Ar(4d) + Xe* → Xe ⁺ + Ar + e	$2.0 \times 10^{-10} T_n^{-1/2}$	est. ^g	
Ar ⁺ + Xe → Xe ⁺ + Ar	$4.3 \times 10^{-13} T_n^{-1/2}$	est.	^f
Ar ⁺ + Xe* → Xe ⁺ + Ar	$4.3 \times 10^{-13} T_n^{-1/2}$	est. ^g	
Xe(1s ₅) + Ar → Xe(1s ₄) + Ar	$0.6 \times 10^{-15} T_n^{-1/2} \exp(-1405/T_g)$	est.	- 0.12
Xe(1s ₄) + Ar → Xe(1s ₅) + Ar	$1 \times 10^{-15} T_n^{-1/2}$	est.	0.12
Xe(1s ₅) + Ar → Xe(1s ₃) + Ar	$0.9 \times 10^{-14} T_n^{-1/2} \exp(-13,122/T_g)$	est.	- 1.13
Xe(6p)M + Ar → Xe(1s ₅) + Ar	$4.5 \times 10^{-14} T_n^{-1/2}$	est.	1.13
Xe(1s ₅) + Ar → Xe(1s ₂) + Ar	$2.7 \times 10^{-14} T_n^{-1/2} \exp(-14,544/T_g)$	est.	- 1.25
Xe(1s ₂) + Ar → Xe(1s ₅) + Ar	$4.5 \times 10^{-14} T_n^{-1/2}$	est.	1.25
Xe(1s ₃) + Ar → Xe(1s ₂) + Ar	$7.5 \times 10^{-13} T_n^{-1/2} \exp(-1421/T_g)$	est.	- 0.12
Xe(1s ₂) + Ar → Xe(1s ₃) + Ar	$2.5 \times 10^{-13} T_n^{-1/2}$	est.	0.12
Xe(1s ₂) + Ar → Xe(6p) + Ar	$1.67 \times 10^{-11} T_n^{-1/2} \exp(-120/T_g)$	est.	- 0.01
Xe(6p) + Ar → Xe(1s ₂) + Ar	$1.0 \times 10^{-11} T_n^{-1/2}$	est.	0.01
Xe(1s ₃) + Ar → Xe(6p) + Ar	$1.85 \times 10^{-11} T_n^{-1/2} \exp(-1620/T_g)$	est.	- 0.13
Xe(6p) + Ar → Xe(1s ₃) + Ar	$3.7 \times 10^{-12} T_n^{-1/2}$	est.	0.13
Xe(6p) + Ar → Xe(3p) + Ar	$4.2 \times 10^{-11} T_n^{-1/2} \exp(-15,300/T_g)$	est.	- 1.32
Xe(3p) + Ar → Xe(6p) + Ar	$4.2 \times 10^{-11} T_n^{-1/2}$	est.	1.32
Xe(6p) + Ar → Xe(5d) + Ar	$9.5 \times 10^{-12} T_n^{-1/2} \exp(-3594/T_g)$	est.	- 0.31
Xe(5d) + Ar → Xe(6p) + Ar	$9.5 \times 10^{-11} T_n^{-1/2}$	est.	0.31
Ar(1s ₅) + Xe → Ar(1s ₄) + Xe	$1.5 \times 10^{-15} T_n^{-1/2} \exp(-881/T_g)$	est.	- 0.076
Ar(1s ₄) + Xe → Ar(1s ₅) + Xe	$2.5 \times 10^{-15} T_n^{-1/2}$	est.	0.076
Ar(1s ₅) + Xe → Ar(1s ₃) + Xe	$0.5 \times 10^{-15} T_n^{-1/2} \exp(-2029/T_g)$	est.	- 0.175
Ar(1s ₃) + Xe → Ar(1s ₅) + Xe	$2.5 \times 10^{-15} T_n^{-1/2}$	est.	0.175
Ar(1s ₅) + Xe → Ar(1s ₂) + Xe	$1.5 \times 10^{-15} T_n^{-1/2} \exp(-3246/T_g)$	est.	- 0.280
Ar(1s ₂) + Xe → Ar(1s ₅) + Xe	$2.5 \times 10^{-15} T_n^{-1/2}$	est.	0.280
Ar(1s ₄) + Xe → Ar(1s ₃) + Xe	$0.83 \times 10^{-15} T_n^{-1/2} \exp(-1148/T_g)$	est.	- 0.099
Ar(1s ₃) + Xe → Ar(1s ₄) + Xe	$2.5 \times 10^{-15} T_n^{-1/2}$	est.	0.099
Ar(1s ₄) + Xe → Ar(1s ₂) + Xe	$2.5 \times 10^{-15} T_n^{-1/2} \exp(-2365/T_g)$	est.	- 0.204
Ar(1s ₂) + Xe → Ar(1s ₄) + Xe	$2.5 \times 10^{-15} T_n^{-1/2}$	est.	0.204
Ar(1s ₃) + Xe → Ar(1s ₂) + Xe	$7.5 \times 10^{-15} T_n^{-1/2} \exp(-1217/T_g)$	est.	- 0.105
Ar(1s ₂) + Xe → Ar(1s ₃) + Xe	$2.5 \times 10^{-15} T_n^{-1/2}$	est.	0.105

^a Rate coefficients have units of $\text{cm}^3 \text{s}^{-1}$ unless noted. T_e is electron temperature (eV). T_g is gas temperature (K), T_n is normalized gas temperature ($T_g/300 \text{ K}$). $-\Delta H$ is the contribution to gas heating (eV).

^b Photoionization cross sections for higher levels were scaled from that of the metastable state based on energy of the ejected electron.

^c Rate shown is for emission. Absorption is addressed using a radiation trapping factor. (See text.)

^d Cross section is for forward reaction. Reverse cross section obtained by detailed balance.

^e The rate of heating by elastic collisions is $k_m(3/2)k_B(2m_e/M)(T_e - T_g)$ eV $\text{cm}^3 \text{s}^{-1}$, for elastic rate coefficient k_m , electron mass m_e , neutral mass M , and Boltzmann's constant k_B .

^f The rate of gas heating of the neutral by charge exchange is $k_{ce}(3/2)k_B(T_{ion} - T_g)$ eV $\text{cm}^3 \text{s}^{-1}$, for charge exchange rate coefficient k_{ce} and ion temperature T_{ion} .

^g Xe* represents any Xe excited state.

^h Estimated based on an average radiative decay rate from the manifold of excited states.

ⁱ Rate coefficient obtained by detailed balancing.

Table 3. Reaction mechanism for He/Ar plasmas.

Species						
Ar	Ar(1s ₅)	Ar(1s ₄)	Ar(1s ₃)	Ar(1s ₂)	Ar(4p)	Ar
Ar(4d)	Ar ⁺	Ar ₂ [*]	Ar ₂ ⁺			Ar(4d)
He	He(2 ³ S)	He(2 ¹ S)	He(2 ³ P)	He(2 ¹ P)	He(3s)	He
He(3p)	He ₂ [*]	He ⁺	He ₂ ⁺	e		He(3p)
<i>hν</i> _{105nm}	<i>hν</i> _{107nm}	<i>hν</i> _{121nm}	<i>hν</i> _{58nm}			<i>hν</i> _{105nm}
Reactions (Note: Reactions involving only Ar species are listed in table 1.)						
Process	Rate coefficient ^a			Reference	− Δ <i>H</i> (eV) ^a	
<i>Photoionization</i>						
<i>hν</i> _{58nm} + Ar → Ar ⁺ + e	3.5 × 10 ^{−17} cm ²			[42] ^b		
<i>hν</i> _{58nm} + Ar(1s ₅) → Ar ⁺ + e	5.9 × 10 ^{−20} cm ²			[42] ^b		
<i>hν</i> _{58nm} + Ar(1s ₄) → Ar ⁺ + e	5.9 × 10 ^{−20} cm ²			[42] ^b		
<i>hν</i> _{58nm} + Ar(1s ₃) → Ar ⁺ + e	5.9 × 10 ^{−20} cm ²			[42] ^b		
<i>hν</i> _{58nm} + Ar(1s ₂) → Ar ⁺ + e	5.9 × 10 ^{−20} cm ²			[42] ^b		
<i>hν</i> _{58nm} + Ar(4p) → Ar ⁺ + e	5.5 × 10 ^{−20} cm ²			[42] ^b		
<i>hν</i> _{58nm} + Ar(4d) → Ar ⁺ + e	5.0 × 10 ^{−20} cm ²			[42] ^b		
<i>hν</i> _{58nm} + He(2 ³ S) → He ⁺ + e	4.66 × 10 ^{−19} cm ²			[42] ^b		
<i>hν</i> _{58nm} + He(2 ¹ S) → He ⁺ + e	4.34 × 10 ^{−19} cm ²			[42] ^b		
<i>hν</i> _{58nm} + He(2 ³ P) → He ⁺ + e	4.34 × 10 ^{−19} cm ²			[42] ^b		
<i>hν</i> _{58nm} + He(2 ¹ P) → He ⁺ + e	4.34 × 10 ^{−19} cm ²			[42] ^b		
<i>hν</i> _{58nm} + He(3s) → He ⁺ + e	4.34 × 10 ^{−19} cm ²			[42] ^b		
<i>hν</i> _{58nm} + He(3p) → He ⁺ + e	4.34 × 10 ^{−19} cm ²			[42] ^b		
<i>hν</i> _{105nm} + He(2 ³ S) → He ⁺ + e	1.51 × 10 ^{−18} cm ²			[42] ^b		
<i>hν</i> _{105nm} + He(2 ¹ S) → He ⁺ + e	1.35 × 10 ^{−18} cm ²			[42] ^b		
<i>hν</i> _{105nm} + He(2 ³ P) → He ⁺ + e	1.28 × 10 ^{−18} cm ²			[42] ^b		
<i>hν</i> _{105nm} + He(2 ¹ P) → He ⁺ + e	1.23 × 10 ^{−18} cm ²			[42] ^b		
<i>hν</i> _{105nm} + He(3s) → He ⁺ + e	1.02 × 10 ^{−18} cm ²			[42] ^b		
<i>hν</i> _{105nm} + He(3p) → He ⁺ + e	0.98 × 10 ^{−18} cm ²			[42] ^b		
<i>hν</i> _{107nm} + He(2 ³ S) → He ⁺ + e	1.53 × 10 ^{−18} cm ²			[42] ^b		
<i>hν</i> _{107nm} + He(2 ¹ S) → He ⁺ + e	1.36 × 10 ^{−18} cm ²			[42] ^b		
<i>hν</i> _{107nm} + He(2 ³ P) → He ⁺ + e	1.29 × 10 ^{−18} cm ²			[42] ^b		
<i>hν</i> _{107nm} + He(2 ¹ P) → He ⁺ + e	1.24 × 10 ^{−18} cm ²			[42] ^b		
<i>hν</i> _{107nm} + He(3s) → He ⁺ + e	1.03 × 10 ^{−18} cm ²			[42] ^b		
<i>hν</i> _{107nm} + He(3p) → He ⁺ + e	0.99 × 10 ^{−18} cm ²			[42] ^b		
<i>hν</i> _{121nm} + He(2 ³ S) → He ⁺ + e	1.95 × 10 ^{−18} cm ²			[42] ^b		
<i>hν</i> _{121nm} + He(2 ¹ S) → He ⁺ + e	1.72 × 10 ^{−18} cm ²			[42] ^b		
<i>hν</i> _{121nm} + He(2 ³ P) → He ⁺ + e	1.63 × 10 ^{−18} cm ²			[42] ^b		
<i>hν</i> _{121nm} + He(2 ¹ P) → He ⁺ + e	1.56 × 10 ^{−18} cm ²			[42] ^b		
<i>hν</i> _{121nm} + He(3s) → He ⁺ + e	1.24 × 10 ^{−18} cm ²			[42] ^b		
<i>hν</i> _{121nm} + He(3p) → He ⁺ + e	1.20 × 10 ^{−18} cm ²			[42] ^b		
<i>Radiative transitions</i>						
He(2 ¹ P) ↔ He	1.8 × 10 ⁹ s ^{−1}			[58] ^c		
He(2 ³ P) → He(2 ³ S)	1.02 × 10 ⁷ s ^{−1}			[58]		
He(3p) → He(2 ³ S)	9.47 × 10 ⁶ s ^{−1}			[58]		
He(3p) → He(2 ¹ S)	1.34 × 10 ⁷ s ^{−1}			[58]		
He(3s) → He(2 ³ P)	1.55 × 10 ⁷ s ^{−1}			[58]		
He(3s) → He(2 ¹ P)	1.83 × 10 ⁷ s ^{−1}			[58]		
<i>Electron impact processes</i>						
e + He → He + e				[61]	e	
e + He ↔ He(2 ³ S) + e	d			[61]		
e + He ↔ He(2 ¹ S) + e	d			[61]		
e + He ↔ He(2 ³ P) + e	d			[61]		

(Continued)

Table 3. (Continued)

Reactions (Note: Reactions involving only Ar species are listed in table 1.)			
Process	Rate coefficient ^a	Reference	$-\Delta H$ (eV) ^a
<i>Photoionization</i>			
$e + \text{He} \leftrightarrow \text{He}(2^1\text{P}) + e$	d	[61]	
$e + \text{He} \leftrightarrow \text{He}(3\text{s}) + e$	d	[61]	
$e + \text{He} \leftrightarrow \text{He}(3\text{p}) + e$	d	[61]	
$e + \text{He} \rightarrow \text{He}^+ + e + e$		[61]	
$e + \text{He}(2^3\text{S}) \leftrightarrow \text{He}(2^1\text{S}) + e$	d	[61]	
$e + \text{He}(2^3\text{S}) \leftrightarrow \text{He}(2^3\text{P}) + e$	d	[61]	
$e + \text{He}(2^3\text{S}) \leftrightarrow \text{He}(2^1\text{P}) + e$	d	[61]	
$e + \text{He}(2^3\text{S}) \leftrightarrow \text{He}(3\text{s}) + e$	d	[61]	
$e + \text{He}(2^3\text{S}) \leftrightarrow \text{He}(3\text{p}) + e$	d	[61]	
$e + \text{He}(2^3\text{S}) \rightarrow \text{He}^+ + e + e$	d	[51]	
$e + \text{He}(2^1\text{S}) \leftrightarrow \text{He}(2^3\text{P}) + e$	d	[61]	
$e + \text{He}(2^1\text{S}) \leftrightarrow \text{He}(2^1\text{P}) + e$	d	[61]	
$e + \text{He}(2^1\text{S}) \leftrightarrow \text{He}(3\text{s}) + e$	d	[61]	
$e + \text{He}(2^1\text{S}) \leftrightarrow \text{He}(3\text{p}) + e$	d	[61]	
$e + \text{He}(2^1\text{S}) \rightarrow \text{He}^+ + e + e$	d	[51]	
$e + \text{He}(2^3\text{P}) \leftrightarrow \text{He}(2^1\text{P}) + e$	d	[61]	
$e + \text{He}(2^3\text{P}) \leftrightarrow \text{He}(3\text{s}) + e$	d	[61]	
$e + \text{He}(2^3\text{P}) \leftrightarrow \text{He}(3\text{p}) + e$	d	[61]	
$e + \text{He}(2^3\text{P}) \rightarrow \text{He}^+ + e + e$	d	[51]	
$e + \text{He}(2^1\text{P}) \leftrightarrow \text{He}(3\text{s}) + e$	d	[61]	
$e + \text{He}(2^1\text{P}) \leftrightarrow \text{He}(3\text{p}) + e$	d	[61]	
$e + \text{He}(2^1\text{P}) \rightarrow \text{He}^+ + e + e$	d	[51]	
$e + \text{He}(3\text{s}) \leftrightarrow \text{He}(3\text{p}) + e$	d	[61]	
$e + \text{He}(3\text{s}) \rightarrow \text{He}^+ + e + e$	d	[51]	
$e + \text{He}(3\text{p}) \rightarrow \text{He}^+ + e + e$	d	[51]	
$e + e + \text{He}^+ \rightarrow \text{He}(2^3\text{S}) + e$	$2.69 \times 10^{-26} T_e^{-4}$	[62, 63]	
$e + \text{He}^+ \rightarrow \text{He}(2^3\text{S})$	$6.76 \times 10^{-13} T_e^{-1/2}$	[52]	
$e + \text{He}^+ + \text{He} \rightarrow \text{He}(2^3\text{S}) + \text{He}$	$1.20 \times 10^{-33} T_e^{-4}$	[52]	
$e + \text{He}_2^+ \rightarrow \text{He}(2^3\text{S}) + \text{He}$	$1.6 \times 10^{-9} T_e^{-1/2}$	[64]	
$e + e + \text{He}_2^+ \rightarrow \text{He}(2^3\text{S}) + \text{He} + e$	$4.5 \times 10^{-25} T_e^{-1/2}$	[62, 63]	
$e + e + \text{He}_2^+ \rightarrow \text{He}_2^* + e$	$1.35 \times 10^{-26} T_e^{-4}$	[62, 63]	
$e + \text{He}_2^+ + \text{He} \rightarrow \text{He}(2^3\text{S}) + \text{He} + \text{He}$	$1.29 \times 10^{-28} T_e^{-1}$	[62, 63]	
$e + \text{He}_2^* \rightarrow \text{He} + \text{He} + e$	3.8×10^{-9}	[62]	
<i>Heavy particle processes</i>			
$\text{He}^+ + \text{He} \rightarrow \text{He}^+ + \text{He}$	6.08×10^{-10}	[53]	^f
$\text{He}^* + \text{He}^* \rightarrow \text{He}^+ + \text{He} + e$	$4.5 \times 10^{-10} T_n^{1/2}$	[62, 63] ^g	
$\text{He}^* + \text{He}^* \rightarrow \text{He}_2^+ + e$	$1.05 \times 10^{-9} T_n^{1/2}$	[62, 63] ^g	
$\text{He}^* + \text{He}_2^* \rightarrow \text{He}^+ + \text{He} + \text{He} + e$	$2.25 \times 10^{-11} T_n^{1/2}$	[62, 63] ^g	
$\text{He}^* + \text{He}_2^* \rightarrow \text{He}_2^+ + \text{He} + e$	$1.28 \times 10^{-10} T_n^{1/2}$	[62, 63] ^g	
$\text{He}_2^* + \text{He}_2^* \rightarrow \text{He}^+ + 3\text{He} + e$	$2.25 \times 10^{-11} T_n^{1/2}$	[62, 63]	
$\text{He}_2^* + \text{He}_2^* \rightarrow \text{He}_2^+ + 2\text{He} + e$	$1.28 \times 10^{-10} T_n^{1/2}$	[62, 63]	
$\text{He}^+ + \text{He} + \text{He} \rightarrow \text{He}_2^+ + \text{He}$	$1.10 \times 10^{-31} T_n^{-0.38} \text{cm}^6 \text{s}^{-1}$	[56]	
$\text{He} + \text{He}_2^* \rightarrow \text{He} + \text{He} + \text{He}$	1.5×10^{-15}	[65]	
$\text{He}^* + \text{He} + \text{He} \rightarrow \text{He}_2^* + \text{He}$	$2 \times 10^{-34} \text{cm}^6 \text{s}^{-1}$	[63, 66] ^g	
<i>Ar and He Heavy Particle Processes</i>			
$\text{He}^+ + \text{He} + \text{Ar} \rightarrow \text{He}_2^+ + \text{Ar}$	$1.10 \times 10^{-31} T_n^{-0.38} \text{cm}^6 \text{s}^{-1}$	[56]	
$\text{He}^* + \text{He} + \text{Ar} \rightarrow \text{He}_2^* + \text{Ar}$	$2.0 \times 10^{-34} \text{cm}^6 \text{s}^{-1}$	[63, 66] ^g	
$\text{He}(2^3\text{S}) + \text{Ar}^{0*} \rightarrow \text{Ar}^+ + \text{He} + e$	$6.75 \times 10^{-10} \exp(-684/T_g)$	[67] ^g	

(Continued)

Table 3. (Continued)

Reactions (Note: Reactions involving only Ar species are listed in table 1.)			
Process	Rate coefficient ^a	Reference	$-\Delta H$ (eV) ^a
<i>Photoionization</i>			
He(2 ¹ S) + Ar ^{0*} → Ar ⁺ + He + e	$2.07 \times 10^{-9} \exp(-684/T_g)$	[67, 68] ^g	
He(2 ³ P) + Ar ^{0*} → Ar ⁺ + He + e	$2.07 \times 10^{-9} \exp(-684/T_g)$	[67, 68] ^g	
He(2 ¹ P) + Ar ^{0*} → Ar ⁺ + He + e	$2.07 \times 10^{-9} \exp(-684/T_g)$	[67, 68] ^g	
He(3s) + Ar ^{0*} → Ar ⁺ + He + e	$2.07 \times 10^{-9} \exp(-684/T_g)$	[67, 68] ^g	
He(3p) + Ar ^{0*} → Ar ⁺ + He + e	$2.07 \times 10^{-9} \exp(-684/T_g)$	[67, 68] ^g	
He ₂ [*] + Ar ^{0*} → Ar ⁺ + He + He + e	1×10^{-10}	est. ^g	
He ⁺ + Ar ^{0*} → Ar ⁺ + He	$5 \times 10^{-14} T_n^{1/2}$	[69, 70] ^g	f
He ₂ ⁺ + Ar ^{0*} → Ar ⁺ + He + He	$2 \times 10^{-10} T_n^{1/2}$	[71] ^g	
He + Ar(1s ₅) → Ar(1s ₄) + He	$1.5 \times 10^{-15} T_n^{1/2} \exp(-881.2/T_g)$	est.	
He + Ar(1s ₄) → Ar(1s ₅) + He	$2.5 \times 10^{-15} T_n^{1/2}$	est.	0.07
He + Ar(1s ₅) → Ar(1s ₃) + He	$0.5 \times 10^{-15} T_n^{1/2} \exp(-2029/T_g)$	est.	
He + Ar(1s ₃) → Ar(1s ₅) + He	$2.5 \times 10^{-15} T_n^{1/2}$	est.	0.17
He + Ar(1s ₅) → Ar(1s ₂) + He	$1.5 \times 10^{-15} T_n^{1/2} \exp(-3246/T_g)$	est.	
He + Ar(1s ₂) → Ar(1s ₅) + He	$2.5 \times 10^{-15} T_n^{1/2}$	est.	0.28
He + Ar(1s ₄) → Ar(1s ₃) + He	$0.83 \times 10^{-15} T_n^{1/2} \exp(-1148/T_g)$	est.	
He + Ar(1s ₃) → Ar(1s ₄) + He	$2.5 \times 10^{-15} T_n^{1/2}$	est.	0.10
He + Ar(1s ₄) → Ar(1s ₂) + He	$2.5 \times 10^{-15} T_n^{1/2} \exp(-2365/T_g)$	est.	
He + Ar(1s ₂) → Ar(1s ₄) + He	$2.5 \times 10^{-15} T_n^{1/2}$	est.	0.21
He + Ar(1s ₃) → Ar(1s ₂) + He	$7.5 \times 10^{-15} T_n^{1/2} \exp(-1217/T_g)$	est.	
He + Ar(1s ₂) → Ar(1s ₃) + He	$2.5 \times 10^{-15} T_n^{1/2}$	est.	0.11

^a Rate coefficients have units of $\text{cm}^3 \text{s}^{-1}$ unless noted. T_e is electron temperature (eV). T_g is gas temperature (K), T_n is normalized gas temperature ($T_g/300\text{K}$). $-\Delta H$ is the contribution to gas heating (eV).

^b Photoionization cross sections for higher levels were scaled from that of the metastable state based on energy of the ejected electron.

^c Rate shown is for emission. Absorption is addressed using a radiation trapping factor. (See text.)

^d Cross section is for forward reaction. Reverse cross section obtained by detailed balance.

^e The rate of heating by elastic collisions is $k_m(3/2)k_B(2m_e/M)(T_e - T_g)$ eV $\text{cm}^3 \text{s}^{-1}$, for elastic rate coefficient k_m , electron mass m_e , neutral mass M , and Boltzmann's constant k_B .

^f The rate of gas heating of the neutral by charge exchange is $k_{ce}(3/2)k_B(T_{ion} - T_g)$ eV $\text{cm}^3 \text{s}^{-1}$, for charge exchange rate coefficient k_{ce} and ion temperature T_{ion} .

^g He* represents any He excited state. Ar^{0*} represents any Ar state (including ground state).

Ar(1s₅), which refreshes the density of the Ar(1s₄) and maintains its density about an order of magnitude higher than the Ar(1s₂). The VUV fluxes internal to the plasma are more than 100 times the magnitude of VUV fluxes escaping from the plasma and striking surfaces (see discussion below). The vast majority of the VUV flux internal to the plasma results from the emission, absorption, and re-emission of photons near the center of the lineshape where the optical depth is greatest. The majority of photons escaping the plasma are from the less populated wings of the lineshape. This recirculation of the VUV photons internal to the plasma increases the average VUV flux relative to that observed from the outside.

The electron energy distributions, $f(\epsilon)$, as a function of height at half radius are shown in figure 3(a). The $f(\epsilon)$ are two-temperature distributions with the transition occurring approximately at the inelastic threshold for the Ar(1s_n) manifold. The low-energy temperature, 4.0 eV, is essentially uniform as a function of height due to the high plasma density, which enables electron–electron collisions to efficiently conduct power throughout the chamber. The high-energy temperature

decreases from 2.0 eV at a height of 11 cm to 1.2 eV at 2.4 cm, a consequence of inelastic collisions in the electron transport from the region of maximum power deposition under the coils to lower-power regions in the reactor.

Fluxes of ions and photons are collected on the substrate surface at the bottom of the reactor. The ambipolar-driven ion fluxes Ar⁺ and Ar₂⁺ are calculated and recorded from the FKM. Photon fluxes of the two resonant transitions [Ar(1s₄) → Ar (104.8 nm), Ar(1s₂) → Ar (106.7 nm)] and excimer emission (Ar₂^{*} at 121 nm) are from the RTM. When averaged across the substrate, the ion flux in the base case is $8.1 \times 10^{15} \text{cm}^{-2} \text{s}^{-1}$ and VUV photon flux is $1.1 \times 10^{16} \text{cm}^{-2} \text{s}^{-1}$ with 80% of the VUV flux coming from the Ar(1s₄) → Ar (106.7 nm) transition. This corresponds to 20.5 mW cm^{-2} in the VUV or a power efficiency of about 15%–20% at producing VUV radiation that escapes the plasma. The fluxes of Ar₂⁺ ($2.8 \times 10^{14} \text{cm}^{-2} \text{s}^{-1}$) and of excimer emission are small in comparison due to the lack of 3-body collisions at low pressure. The volume averaged radiation trapping factors are 226 for the Ar(1s₄) → Ar (104.8 nm) transition and 586 for the Ar(1s₂) → Ar (106.7 nm)

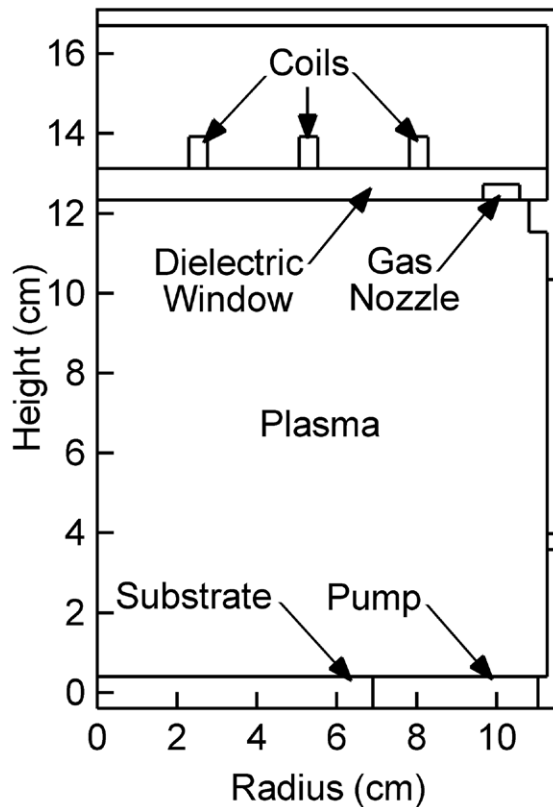


Figure 1. Schematic of the inductively coupled plasma reactor used in the model.

transition. For these conditions, the flux of VUV photons onto the substrate exceeds that of the ions. The magnitude of the VUV fluxes are commensurate to those experimentally measured for similar conditions [14–17].

All excited states of Ar can be photo-ionized by the VUV fluxes. The random VUV fluxes in the middle of the reactor are $2.2 \times 10^{18} \text{ cm}^{-2} \text{ s}^{-1}$, which are comparable to or can exceed the random thermal electron fluxes. However, the cross sections for photoionization of Ar excited states are small, 10^{-19} cm^2 . The end result is that rate of photoionization is small, having a maximum value of $2.4 \times 10^{11} \text{ cm}^{-3} \text{ s}^{-1}$, compared to ionization by bulk electrons having a maximum value of $8.7 \times 10^{15} \text{ cm}^{-3} \text{ s}^{-1}$.

4. Controlling photon fluxes in Ar ICPs

4.1. Photon and ion fluxes versus pressure

To investigate methods to control the relative magnitudes of the ion and photon fluxes, we varied the pressure from 5 to 50 mTorr while keeping other conditions the same as the base case. The photon and ion fluxes to the bottom substrate as a function of pressure are shown in figure 4. Representative line-shape functions and radiation trapping factors are in figure 5. For these conditions, total VUV fluxes monotonically increase while asymptotically approaching a maximum at higher pressures of $1.5 \times 10^{16} \text{ cm}^{-2} \text{ s}^{-1}$ (or 28 mW cm^{-2}). Ion fluxes onto the substrate are maximum at low pressure and decrease

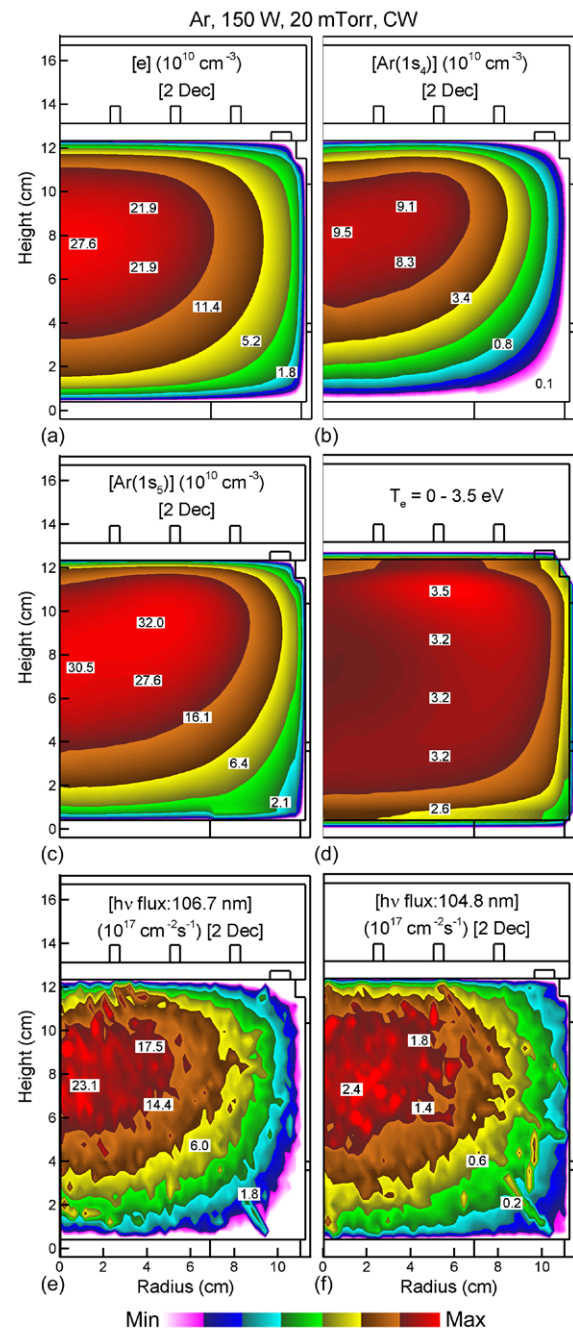


Figure 2. Time-averaged plasma properties under base case conditions (Ar, 20 mTorr, 200 sccm, 10 MHz, 150 W cw). (a) Electron density, (b) resonant Ar(1s₄) density, (c) metastable Ar(1s₅) density, (d) electron temperature, (e) random VUV fluxes for 106.8 nm and (f) for 104.8 nm. The densities are on 2-decade log scales.

monotonically with increasing pressure. These trends in both ion and photon fluxes are somewhat artificial since fluxes are recorded on the lower substrate where, for example, a wafer may be located. With increasing pressure, the source function for ionization becomes progressively more confined to the skin depth of the electromagnetic field below the insulator, and so moves closer to the top surface. The loss of ions is therefore preferentially to the top surface at higher pressures. At low pressures, the skin depth is anomalous, resulting in

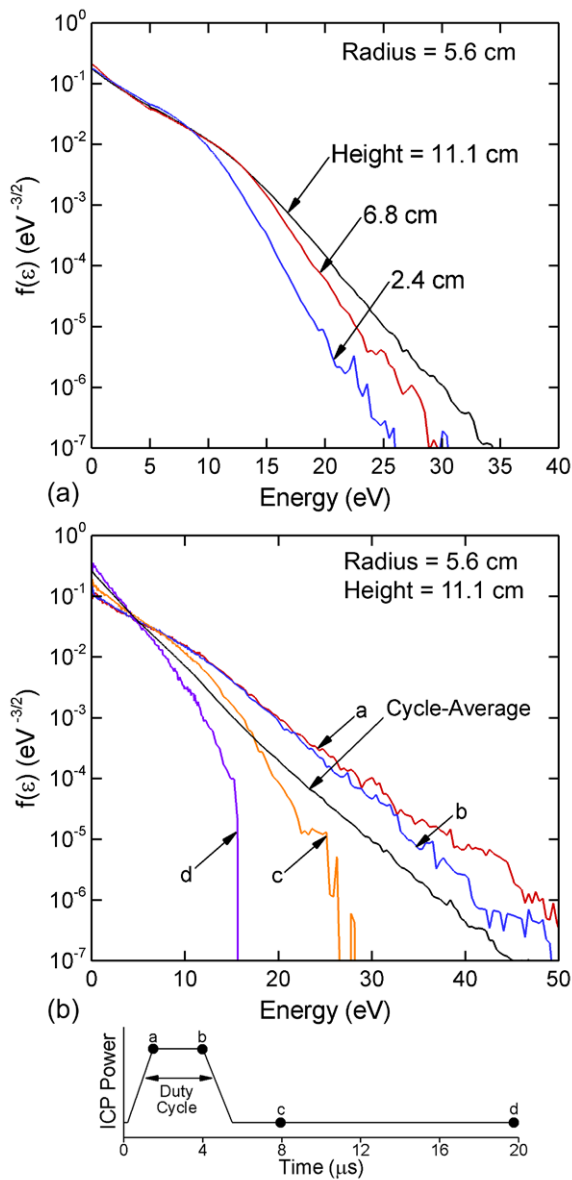


Figure 3. Electron energy distributions at a radius of 5.6 cm and different vertical locations for the base case conditions (Ar, 20 mTorr, 200 sccm, 10 MHz, 150 W cw).

high-energy electrons and the ionization sources being more uniformly distributed in the reactor. This results in the ion flux onto the substrate decreasing on a relative basis compared to other surfaces when the pressure increases.

The monotonic, but saturating, increase in the VUV flux onto the substrate for constant power deposition with increasing pressure results from competing effects. In argon ICPs, the electron density and excited densities increase with increasing pressure over this range of pressures [37–39]. However, the shortening of the mean free paths and increase in plasma density which shortens the electromagnetic skin depth localizes the production of VUV photons closer to the top of the reactor near the coils. This localization of the production of VUV photons, more remote from the substrate, might otherwise decrease the VUV flux onto the substrate. At the same time, the higher pressure produces a larger radiation trapping

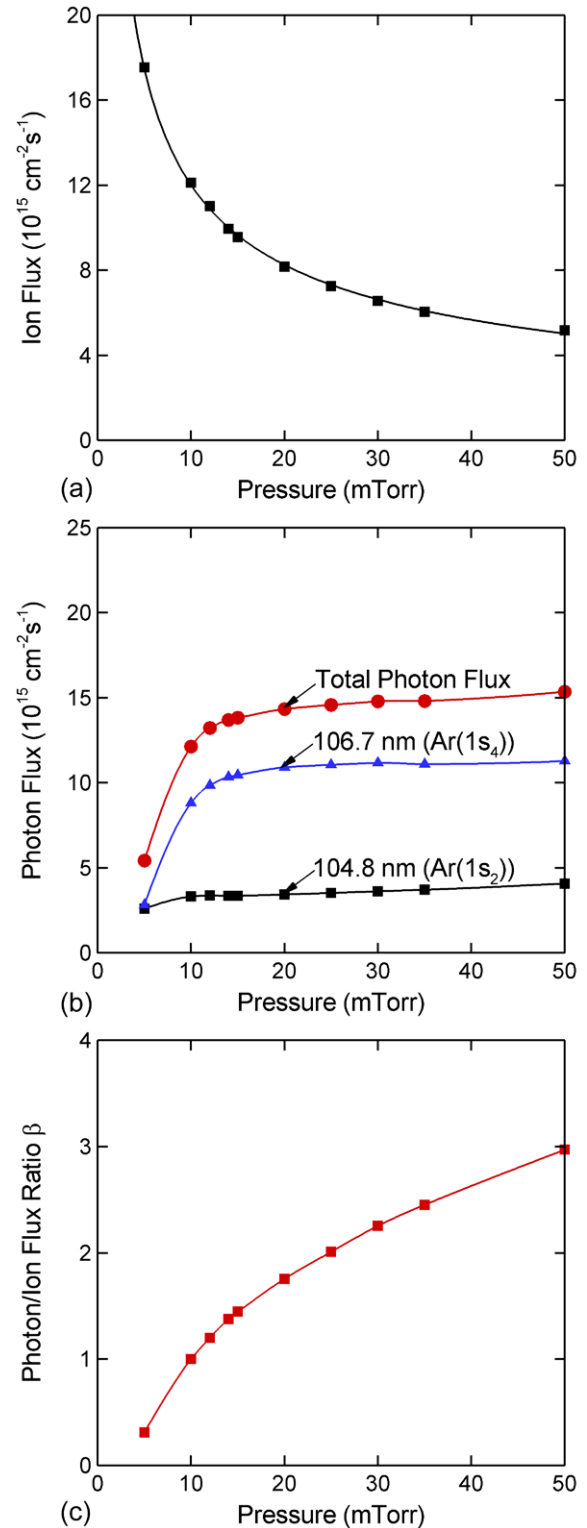


Figure 4. Substrate-averaged fluxes for different pressures in Ar (200 sccm, 10 MHz, 150 W cw). (a) Ion fluxes, (b) photon fluxes, (c) total photon/ion flux ratio. Total photon fluxes are the sum of 106.7 nm and 104.8 nm transitions.

factor that lengthens the lifetime of the radiating states, making those states more susceptible to being quenched by both electron and heavy-particle collisions. For our geometry and operating conditions, the incremental increase in the source of excited states dominates over quenching at lower

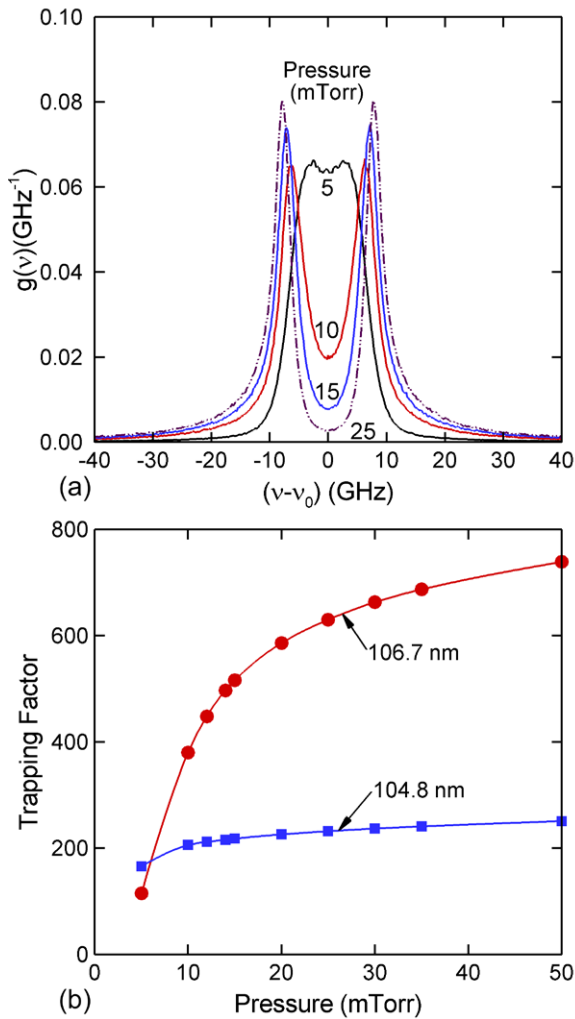


Figure 5. Optical properties for different pressures in Ar (200 sccm, 10 MHz, 150 W cw). (a) Line shape function of 106.7 nm emission. (b) Trapping factor for 106.7 nm and 104.8 nm Ar emission.

pressures and nearly balances the sources at higher pressures. Meanwhile, a constant power ultimately limits the VUV flux that can be generated in the absence of an increase in efficiency of excited state production.

With an increase in photon fluxes and decrease in ion fluxes onto the substrate as a function of pressure, the ratio of the VUV to ion flux incident onto the substrate, β , increases as the pressure increases as shown in figure 4(c). At 5 mTorr, ion fluxes are larger than VUV fluxes and $\beta = 0.3$. As the pressure increases above 10 mTorr, VUV fluxes become larger than ion fluxes onto the substrate, with $\beta = 3.0$ at 50 mTorr.

The lineshape functions for the 106.7 nm transition, shown in figure 5(a), display the transition from moderate trapping at 5 mTorr (trapping factor 115) to severe trapping at 25 mTorr (trapping factor 630). These lineshape functions are for the VUV flux that escapes from the plasma averaged over all surfaces, and so would be the spectrum observed looking into the plasma from the outside. The severity of trapping is indicated by the self absorption at line center. Photons emitted near line center are reabsorbed with a mean free path of $<100 \mu\text{m}$ and are isotropically re-emitted. These photons generally

recirculate within the plasma through hundreds of emissions and reabsorptions until either that quantum of energy is quenched or the photon is statistically emitted in the wings of the lineshape function. Photons emitted in the wings have proportionately longer mean free paths which enable the photons to escape from the plasma. The width of the self-absorbed core of the lineshape function is determined in large part by the Doppler width at low pressure, which for these conditions is 9–10 GHz.

The general trends discussed here for magnitudes of VUV fluxes and ratios of VUV to ion fluxes generally agree with prior experimental measurements [15, 16]. Woodworth *et al* [15] measured VUV fluxes from ICPs sustained in pure Ar at 20 mTorr and 200 W rf power. Their values for VUV fluxes, $3.5 \times 10^{16} \text{cm}^{-2} \text{s}^{-1}$ or 52mW cm^{-2} , at 200 W compare favorably to the results of the simulation, $1.1 \times 10^{16} \text{cm}^{-2} \text{s}^{-1}$ or 20.5mW cm^{-2} at 150 W. Jinnai *et al* also measured VUV fluxes in ICPs sustained in pure Ar at 5 mTorr on the order of 10^{15} – $10^{16} \text{cm}^{-2} \text{s}^{-1}$ [16]. The VUV fluxes from our simulation at 5 mTorr ($5.4 \times 10^{15} \text{cm}^{-2} \text{s}^{-1}$) are in the same range.

A more quantitative comparison to experiment can be made for VUV emission from ICPs sustained in Ar reported by Boffard *et al* [37]. In this work, ICPs were sustained in Ar at pressures of 1 mTorr to 25 mTorr for a power of 600 W. The total flux of VUV emissions (dominated by the transitions at 104.8 nm and 106.7 nm) were measured on the bottom substrate of their reactor using a calibrated VUV photodiode. The geometry and operating conditions of Boffard *et al* were implemented in our model. A comparison to the experimental results is shown in figure 6. In the simulation, photon fluxes were averaged over the substrate, and random thermal ion fluxes were measured in the center of the reactor. The trends of computed results match the experiment. The experimental results show a broad maximum in the VUV flux at 10–12 mTorr whereas the simulation shows the maximum at 15 mTorr. The absolute magnitudes of the VUV fluxes agree to within a factor of 2. Note that the random thermal ion fluxes measured in the center of the reactor increase with increasing pressure whereas the ion fluxes incident onto the substrate decrease as pressure increases.

This comparison to the results of Boffard *et al* emphasizes the importance of geometry in assessing the VUV and ion fluxes onto the substrate. The differences in the pressure dependence of the VUV fluxes shown in figures 5(b) and 6(a) are predominantly a result of geometry since the reaction mechanisms are identical. For example, the VUV photons in these two cases originate in different locations in the reactor with respect to the substrate and so the substrate subtends a different solid angle.

4.2. Pulsing: photon and ion fluxes versus duty cycle (DC)

With cw excitation, the ability to control the ratio of VUV to ion flux is limited. For a given pressure and power deposition there is a single reactor-averaged T_e that produces the steady-state plasma. As a result, the balance between populating the resonant states and ionization is fairly constrained. Pulsed excitation provides additional flexibility since T_e can

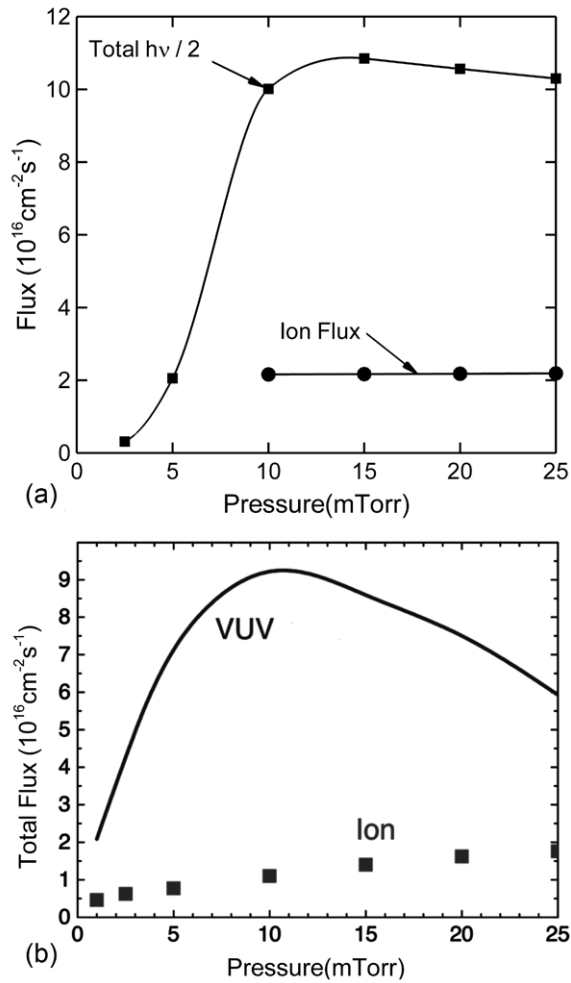


Figure 6. Photon and ion fluxes for the experimental conditions of Boffard *et al* [37] (Ar, 6 sccm, 600 W cw). (a) Simulation and (b) experimental results.

considerably vary during the pulsed cycle and so the ratio of excitation of resonant states and ionization is not constrained to a single reactor-averaged value [6, 40, 41].

With the goal of controlling the average fluxes of VUV photons and ions onto the substrate, we investigated pulsed plasma excitation of the ICP. The pulsed power waveform is characterized by the pulse repetition frequency, PRF, the number of power pulses per second; the duty cycle, DC, the fraction of the pulsed period the ICP power is applied; and the cycle average power deposition, CAP. The base case for pulsing is Ar at 20 mTorr, with a PRF of 50 kHz (20 μ s period), 15% dc and CAP of 150 W.

The electron temperature T_e , ion density, and the density of Ar(1s₄) during the pulse cycle are shown in figures 7–9. During the pulse-on period, T_e spikes to 4.8 eV compared with the cw value of 3.5 eV. This is the overshoot effect [6, 40, 41] where upon applying power to the lower electron density at the end of the preceding afterglow, T_e increases above the cw value in order to avalanche the electron density. Electrons are heated in the skin depth between the coils and convect to the lower part of the reactor. At the trailing edge of the power pulse, T_e decreases to 2.3 eV in the afterglow, nearly uniformly

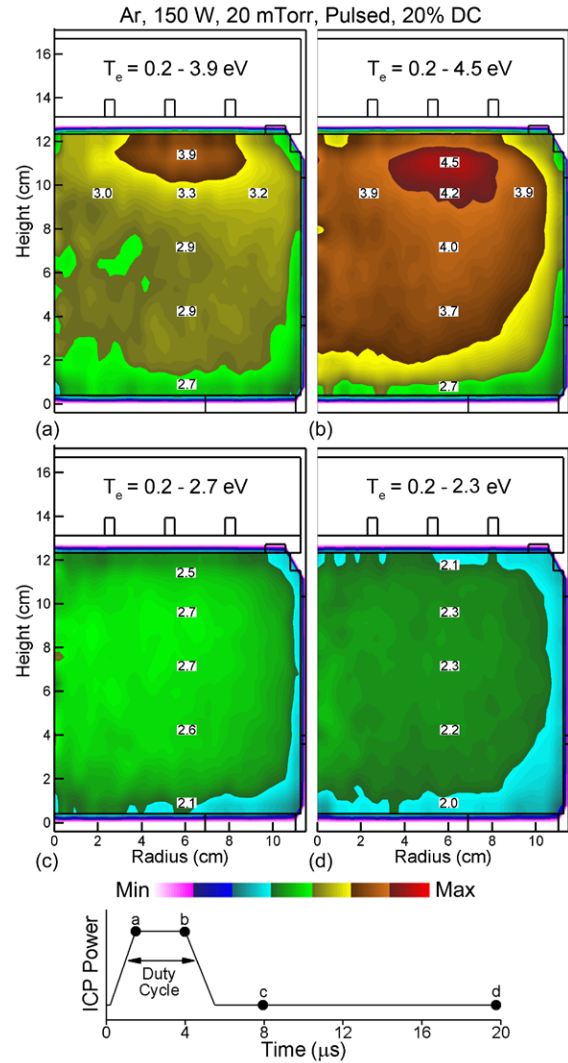


Figure 7. Electron temperature at different times during a pulsed cycle. Plasma conditions are Ar, 20 mTorr, 200 sccm, 10 MHz, 150 W pulsed-period-averaged power, PRF = 50 kHz, duty cycle = 20%. (a) At leading edge of the power-on period, (b) at trailing edge of power-on period, (c) 2.5 μ s into afterglow period, (d) end of afterglow period. These times are indicated in the schematic at the bottom of the figure.

distributed in the reactor. T_e is maintained during the afterglow by super-elastic relaxation of the metastable states of Ar, while thermal conduction provides the uniform distribution.

Electron energy distributions at different times during the pulsed cycle are shown in figure 3(b) at radius of 5.6 cm and height of 11.1 cm at the edge of the skin depth. The time during the pulse period for each plot is shown in the diagram at the bottom of the figure. At the beginning of the pulse, the larger electric field required to avalanche the plasma to higher densities produces an extended high energy tail, which begins to relax during the pulse-on period, producing a two-temperature distribution. At the end of the power-on pulse, the temperature of the bulk and tail are 5.2 eV and 3.3 eV, respectively. The tail of $f(\epsilon)$ rapidly decays at the end of the power pulse while the low-energy portion of the distribution is sustained by super-elastic electron heating of the long-lived metastable states.

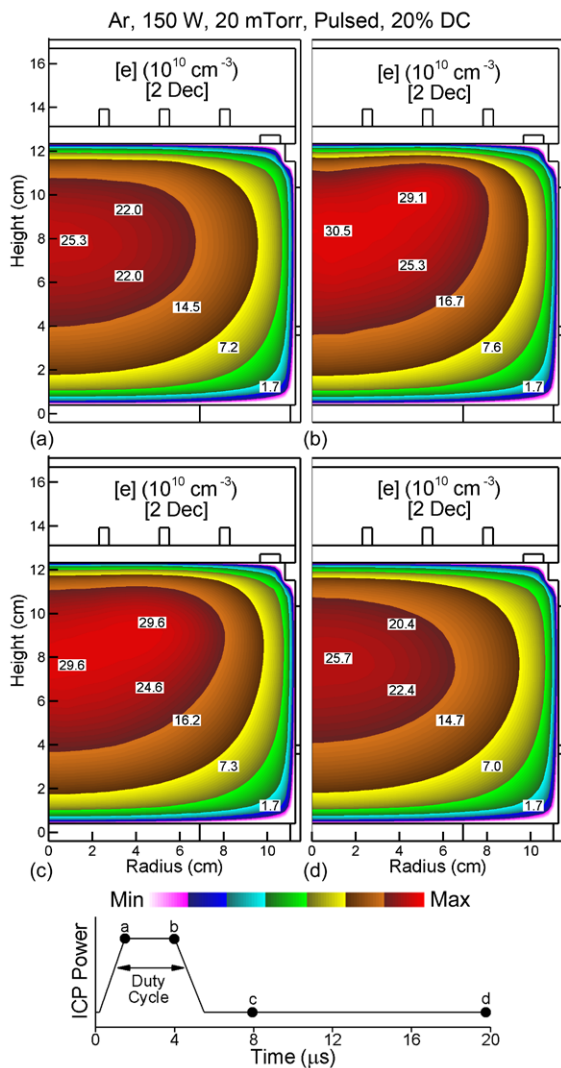


Figure 8. Electron density at different times during a pulsed cycle for the conditions of figure 7 (Ar, 20 mTorr, 200 sccm, 10 MHz, 150 W pulsed-period-averaged power, PRF = 50 kHz, duty cycle = 20%). (a) at leading edge of the power-on period, (b) at trailing edge of power-on period, (c) 2.5 μ s into afterglow period, (d) end of afterglow period. These times are indicated in the schematic at the bottom of the figure. Values are plotted on a 2-decade log scale.

The modulation in T_e also produces a modulation in the electron and Ar^+ densities. The maximum ion density occurs at the end of the power-on pulse, $3.4 \times 10^{11} \text{ cm}^{-3}$. For this PRF, the interpulse period is not long enough to produce significant loss by diffusion during the afterglow, and so the intrapulse modulation in the ion density is small, about 15%. The resonant $\text{Ar}(1s_4)$ state has an intrapulse modulation of about 50%. The relatively long persistence of the resonant state results, in part, from its radiation trapped lifetime of about 5 μ s, and due to mixing with the metastable state $\text{Ar}(1s_5)$ whose density decays slowly due to electron collision quenching and diffusion.

The differences in the decay rates of Ar^+ and $\text{Ar}(1s_4)$ during the pulse period, imply that the ratio of the VUV to ion fluxes incident onto the substrate will vary during the pulse period. For example, the VUV fluxes onto the substrate

as a function of time for different duty cycles are shown in figure 10. The corresponding ion fluxes, ratio of VUV-to-ion flux, β , and electron temperatures are shown in figure 11. The ICP was sustained in Ar at 20 mTorr with a CAP of 150 W for DCs from 10% to 50% and a PRF of 50 kHz. The quasi-dc value of T_e is 3.3 eV, a value that is reached after about 3–4 μ s for the 50% dc. With shorter duty cycle, T_e peaks to a higher value upon application of power, 4.2 eV for 10% DC. This is, in part, a consequence of the higher peak power applied during the shorter cycle to produce the same cycle-averaged power deposition. With the exception of the shortest duty cycle, the T_e at the end of the afterglow period is about 2 eV, largely sustained by super-elastic relaxation. The modulation in the ion flux onto the substrate during the pulsed cycle is about 15–20%.

The modulation in the VUV flux onto the substrate of the 104.8 nm line originating with $\text{Ar}(1s_2)$ is a factor of 15–16 whereas the modulation in the 106.7 nm line originating with the $\text{Ar}(1s_4)$ is a factor of 3–4. The cascade downward of excited states during the afterglow terminates with the $\text{Ar}(1s_5)$ metastable state that is collisionally coupled to the $\text{Ar}(1s_4)$, which has a density of $8\text{--}10 \times 10^{10} \text{ cm}^{-3}$ during the afterglow. This collisional coupling replenishes the $\text{Ar}(1s_4)$ to maintain a density of $1.2\text{--}1.5 \times 10^{10} \text{ cm}^{-3}$ while the trapped optical lifetime is 5 μ s. The end result is that there is significant VUV emission at 106.7 nm after the power is terminated and T_e decreases. The $\text{Ar}(1s_2)$ is efficiently collisionally coupled to $\text{Ar}(1s_3)$ having a density of $8\text{--}10 \times 10^9 \text{ cm}^{-3}$, but less efficiently collisionally coupled to the $\text{Ar}(1s_5)$. The $\text{Ar}(1s_2)$ is therefore less likely to be replenished during afterglow by the reservoir of $\text{Ar}(1s_5)$. The VUV emission at 104.8 nm therefore more closely follows the electron temperature and its trapped lifetime of 0.4 μ s. The ratio of VUV-to-ion flux, β , during the pulse period is highly modulated. The maximum value of β at the end of the power pulse is 2.4 for a 10% DC and 2.0 for a 50% DC. β decreases to 0.6–0.9 at the end of the afterglow, compared to a cw value of $\beta = 1.7$. During most of the pulse period, the VUV flux exceeds the ion flux. However, at the end of the afterglow, ion flux could be larger due to the longer lifetime of ions.

The peak (maximum during the pulse) and cycle-averaged VUV and ion fluxes, and the ratio of VUV-to-ion flux, β , are shown in figure 12 as a function of DC. The VUV fluxes are the sum of the fluxes for the 104.8 and 106.7 nm lines. The peak VUV fluxes increase with decreasing duty cycle by about 10% over a DC drop from 50% to 10%. The peak VUV flux is $2.2 \times 10^{16} \text{ cm}^{-2} \text{ s}^{-1}$ (40.9 mW cm^{-2}) at a DC of 10% compared to the cw value of $1.1 \times 10^{16} \text{ cm}^{-2} \text{ s}^{-1}$ (20.5 mW cm^{-2}). This increase reflects the peaking of the electron temperature to higher temperatures with lower DC. The cycle-averaged VUV flux increases with DC, indicating that the longer power-on period more efficiently produces VUV flux, though with a lower peak flux. The peak and cycle-averaged ion fluxes are essentially constant for different DC values, since the average power deposition is also constant. As a result, as DC increases from 10% to 50%, the peak ratio of VUV to ion fluxes decreases from 2.3 to 2.0 and the average ratio increases from 1.1 to 1.5.

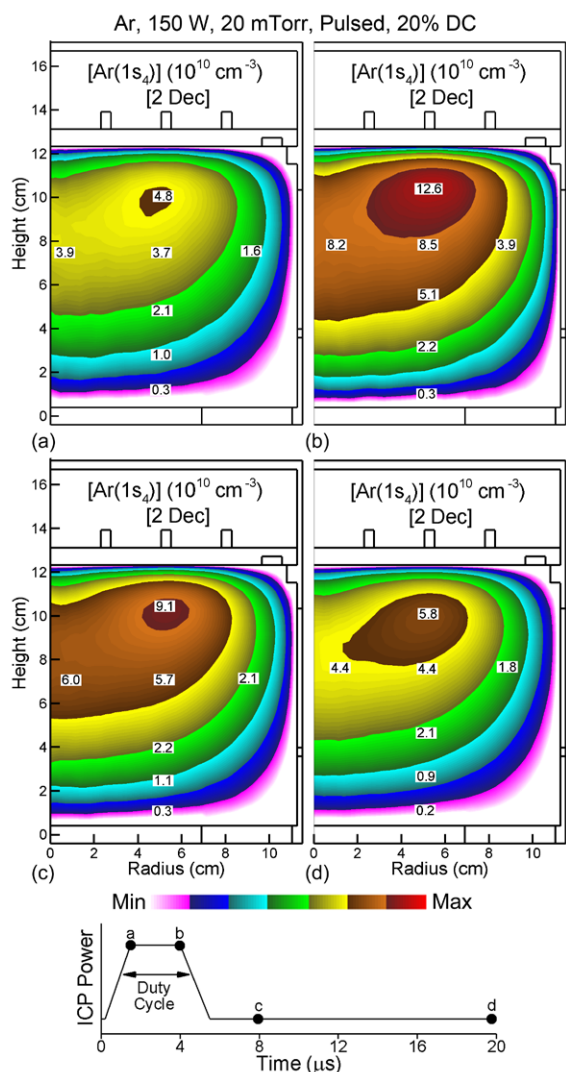


Figure 9. Density of the radiative state $\text{Ar}(1s_4)$ at different times during a pulsed cycle for the conditions of figure 7 (Ar, 20 mTorr, 200 sccm, 10 MHz, 150 W pulsed-period-averaged power, PRF = 50 kHz, duty cycle = 20%). (a) At leading edge of the power-on period, (b) at trailing edge of power-on period, (c) 2.5 μs into afterglow period, (d) end of afterglow period. These times are indicated in the schematic at the bottom of the figure. Values are plotted on a 2-decade log scale.

5. Controlling spectra of photon fluxes in Ar/Xe and He/Ar ICPs

Some coarse control over the VUV spectra obtained from low-pressure ICPs can be obtained by gas mixture. For example, Ar/Xe gas mixtures will produce additional longer wavelength VUV lines at 147.1 nm [$\text{Xe}(1p_4) \rightarrow \text{Xe}(5s^25p^6)$] and 129.76 nm [$\text{Xe}(1p_2) \rightarrow \text{Xe}(5s^25p^6)$]. Ar/He mixtures will produce additional shorter wavelength VUV, predominantly at 59.1 nm [$\text{He}(1s2p^3P^0) \rightarrow \text{He}(1s^2^1S)$]. We first discuss results for Ar/Xe mixtures, where the base case is Ar/Xe = 75/25 at 20 mTorr with 150 W cw ICP power. Densities of Ar^+ and Xe^+ , and the resonant states densities $\text{Ar}(1s_4)$ and $\text{Xe}(1s_4)$ are shown in figure 13. The maximum Xe^+ density is $6.4 \times 10^{11} \text{ cm}^{-3}$ while that of Ar^+ is $4.5 \times 10^{10} \text{ cm}^{-3}$. The

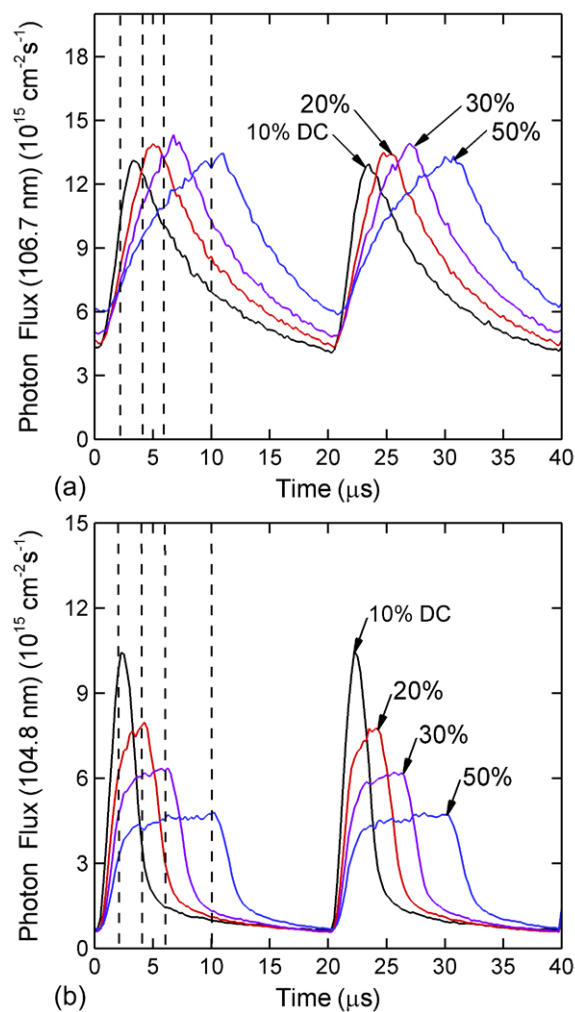


Figure 10. Photon fluxes collected on and averaged over the bottom substrate as a function of time for two discharge pulses for different duty cycles. (a) 106.7 nm (originating from $\text{Ar}(1s_4)$) and (b) 104.8 nm (originating from $\text{Ar}(1s_2)$). The dashed lines indicate the end of power-on period. Plasma conditions are Ar, 20 mTorr, 200 sccm, 10 MHz, 150 W CAP, PRF = 50 kHz.

higher Xe^+ density results from its lower ionization potential compared to Ar (12.1 eV versus 16 eV). The metastable and resonant states of Ar do not have sufficient energy to Penning-ionize Xe, though the $\text{Ar}(4p)$ and $\text{Ar}(4d)$ states are capable of Penning reactions. However, due to the low densities of these states, their contribution to the higher Xe^+ density is not large. The maximum Penning-ionization rates by $\text{Ar}(4p)$ and $\text{Ar}(4d)$ are $3.7 \times 10^{12} \text{ cm}^{-3} \text{ s}^{-1}$ and $7.8 \times 10^{11} \text{ cm}^{-3} \text{ s}^{-1}$ respectively, much larger than photoionization at $5 \times 10^{10} \text{ cm}^{-3} \text{ s}^{-1}$. However these values are small compared to bulk ionization by electron impact, at $1.0 \times 10^{16} \text{ cm}^{-3} \text{ s}^{-1}$. The densities of the resonant states of Ar and Xe are commensurate. The density of $\text{Xe}(1s_4)$ is $1.6 \times 10^{10} \text{ cm}^{-3}$ and that of $\text{Ar}(1s_4)$ is $1.5 \times 10^{10} \text{ cm}^{-3}$. Although the electron impact cross section for excitation of $\text{Xe}(1s_4)$ from ground state has a lower threshold and is 5 times larger than that of $\text{Ar}(1s_4)$, there are few other processes that further discriminate the formation of the two states other than the lower rate of diffusion losses by the heavier Xe atoms.

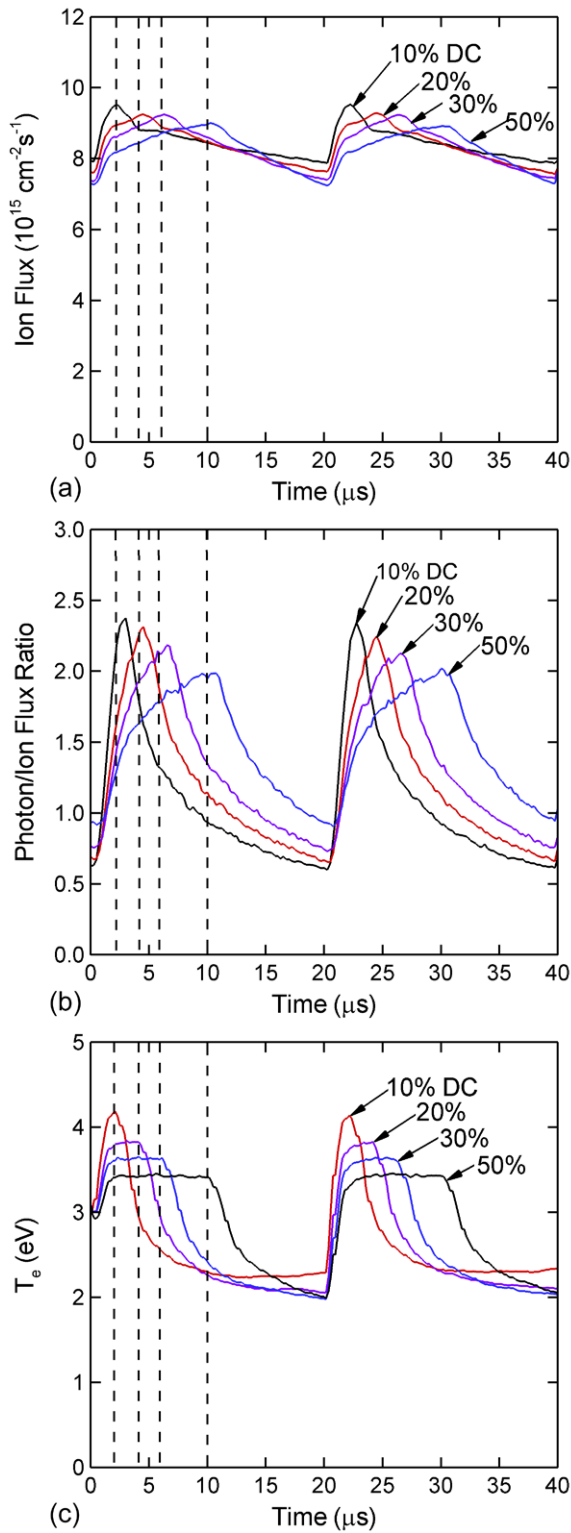


Figure 11. Plasma properties as a function of time for two discharge pulses with different duty cycles. Fluxes are collected on and averaged over the substrate. (a) Ion flux, (b) ratio of total VUV flux to ion flux, (c) electron temperature. Dashed lines indicate the end of power-on period. Plasma conditions are Ar, 20 mTorr, 200 sccm, 10 MHz, 150 W CAP, PRF = 50 kHz.

EEDs at the edge of the electromagnetic skin depth are shown in figure 14(a) for different Xe fractions. For a Xe fraction of 1%, $f(\epsilon)$ is a two-temperature distribution with bulk

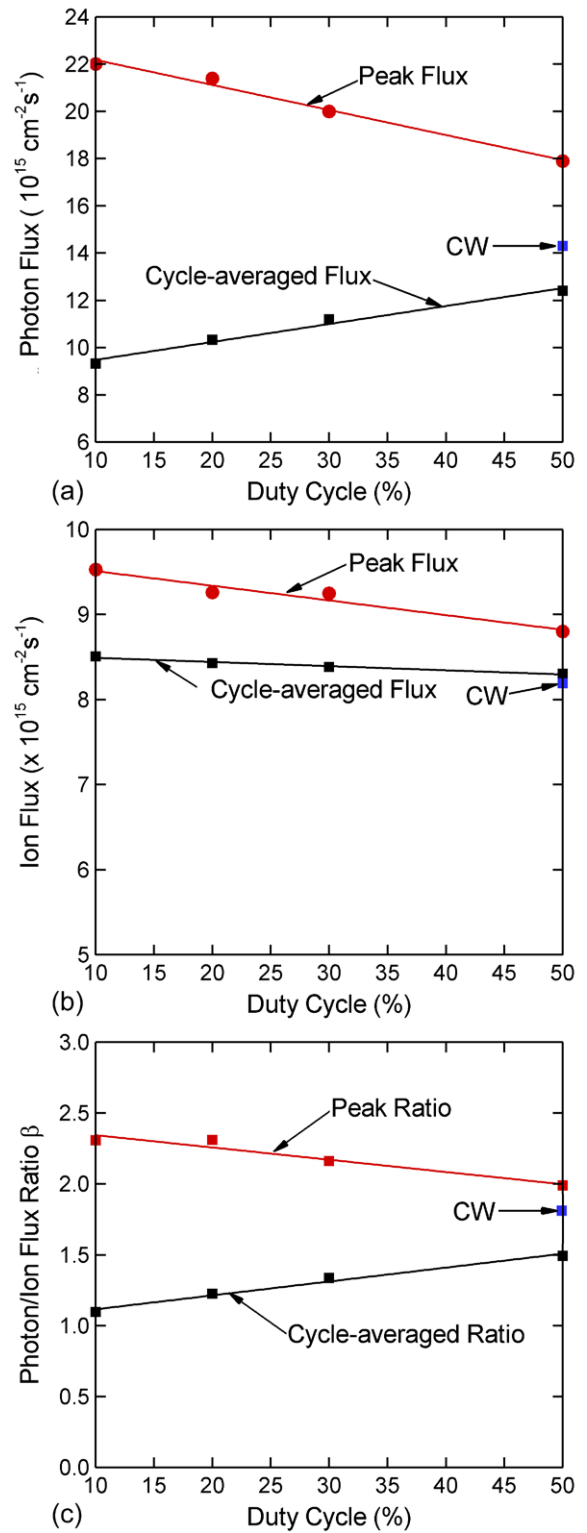


Figure 12. Properties of fluxes striking and averaged over the substrate for pulsed excitation for different duty cycles and for cw excitation. (a) Total VUV photon flux, (b) ion flux, (c) ratio of VUV flux to ion flux. Plasma conditions are Ar, 20 mTorr, 200 sccm, 10 MHz, 150 W CAP, PRF = 50 kHz.

and tail temperatures of 3.0 eV and 2.1 eV. The breakpoint between the temperatures, 11 eV, is approximately the inelastic thresholds for the Ar(4s) manifold. As the Xe fraction increases, $f(\epsilon)$ retains its two-temperature character with the

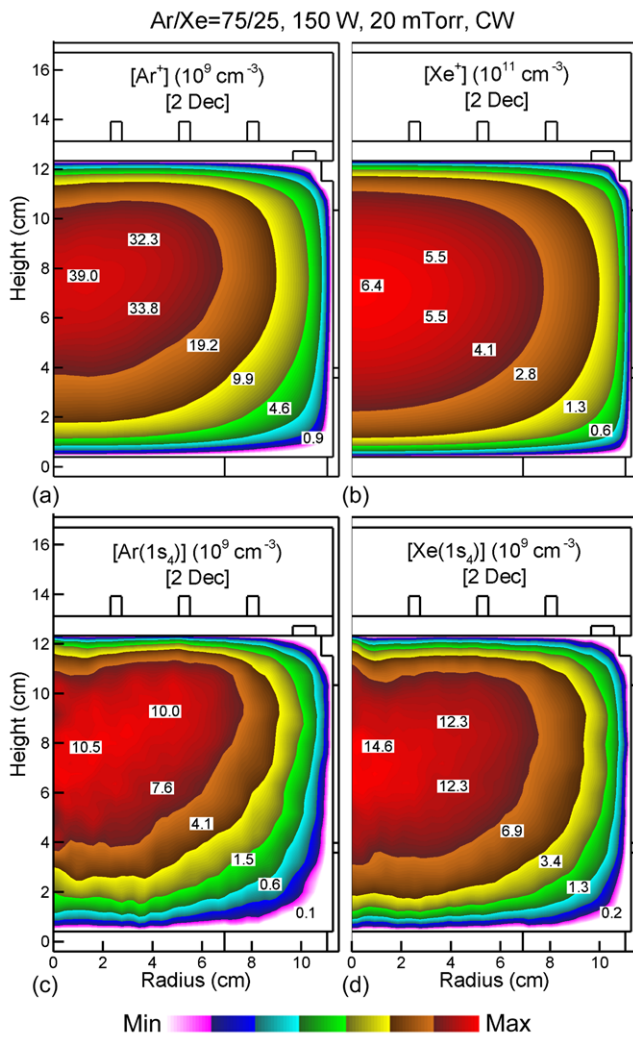


Figure 13. Plasma properties for an Ar/Xe = 75/25 mixture with cw excitation (20 mTorr, 200 sccm, 10 MHz, 150 W). (a) Ar^+ density, (b) Xe^+ density, (c) $\text{Ar}(1s_4)$ resonant state density, and (d) $\text{Xe}(1s_4)$ resonant state densities. The densities are plotted on 2-decade log scales.

transition energy between the two temperatures moving close to the Xe threshold at 8–9 eV. The high-energy tail at large Xe fraction is depleted by the relatively low threshold inelastic collisions of Xe. The bulk and tail values of T_e for a Xe mole fraction of 40% are 2.2 eV and 1.4 eV.

The scaling of VUV intensity as a function of Ar/Xe gas mixture demonstrating coarse spectral control is shown in figure 15(a) for constant power and pressure. The total VUV emission from Ar and Xe (sum of their respective resonant transitions), the total VUV flux and the ratio of VUV flux from Xe compared to total fluxes are shown for Xe fractions up to 40%. The total VUV flux decreases by about 40% as Xe fraction increases from 0 to 40%. This decrease is in part due to the larger proportion of power deposition expended in ionization of Xe relative to excitation compared to Ar. For example, at an electron temperature of 4 eV in pure Ar, about 1% of the power dissipated by electron collisions with the ground state produce ionization, whereas 53% of the power produces excitation of the $\text{Ar}(4s)$ manifold. In pure Xe at 4 eV, 32% of the

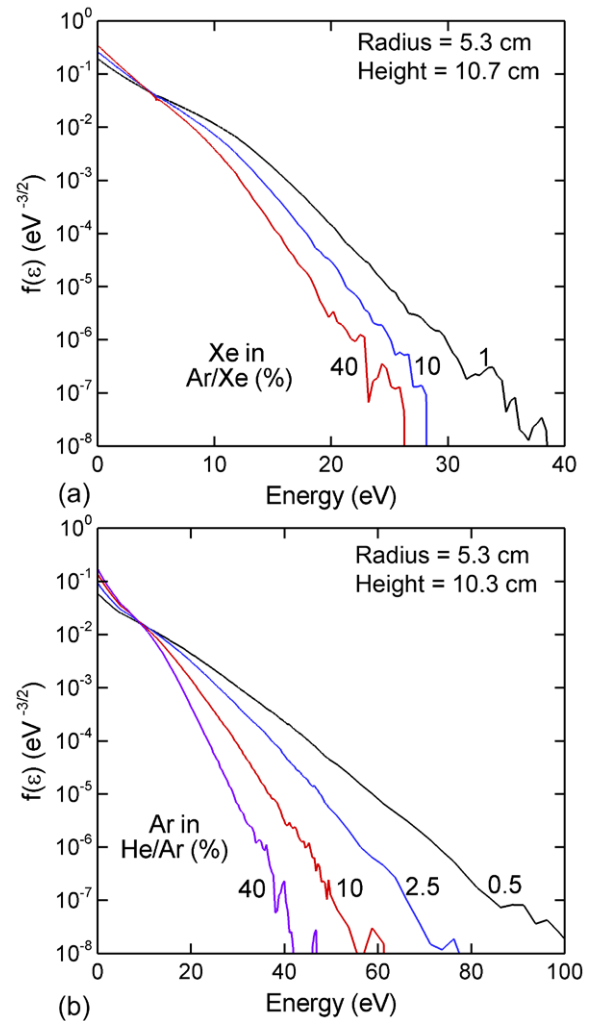


Figure 14. Electron energy distributions in cw ICPs for different gas mixtures. The EEDs are at the edge of skin depth at a radius of 5.3 cm (20 mTorr, 200 sccm, 10 MHz, 150 W). (a) Ar/Xe mixtures with Xe fractions of 1–40% (b) and He/Ar mixtures with Ar fraction of 0.5 to 40%.

power produces ionization and 23% produces excitation of the $\text{Xe}(6s)$ manifold. The higher plasma density with increasing Xe fraction also produces more electron collision quenching of the resonant states. Electron temperature T_e decreases from 3.1 eV with 1% of Xe to 2.1 eV at 40% of Xe.

The proportion of the VUV flux due to emission from Xe increases somewhat linearly with increasing Xe fraction up to 20% before beginning to saturate. With 20% Xe, the fraction of the VUV flux due to Xe emission is 60%. With 40% Xe, the fraction of VUV flux due to Xe emission is 85%. The absolute VUV flux saturates at a Xe fraction of 30%. At this Xe fraction, the majority of power deposition is expended in Xe.

Spectral lineshapes for Ar (106.7 nm) and Xe (147.1 nm) emission and radiation trapping factors are shown in figure 16 for different Xe fractions. The trapping factor for Ar only moderately decreases as the Ar fraction decreases from 99% to 60%. As the Xe fraction increases from 1% to 40%, the trapping factor increases from 58 to 170. The resulting lineshape functions reflect these trends in trapping factor. The lineshape function for Ar 106.7 nm emission is only moderately less

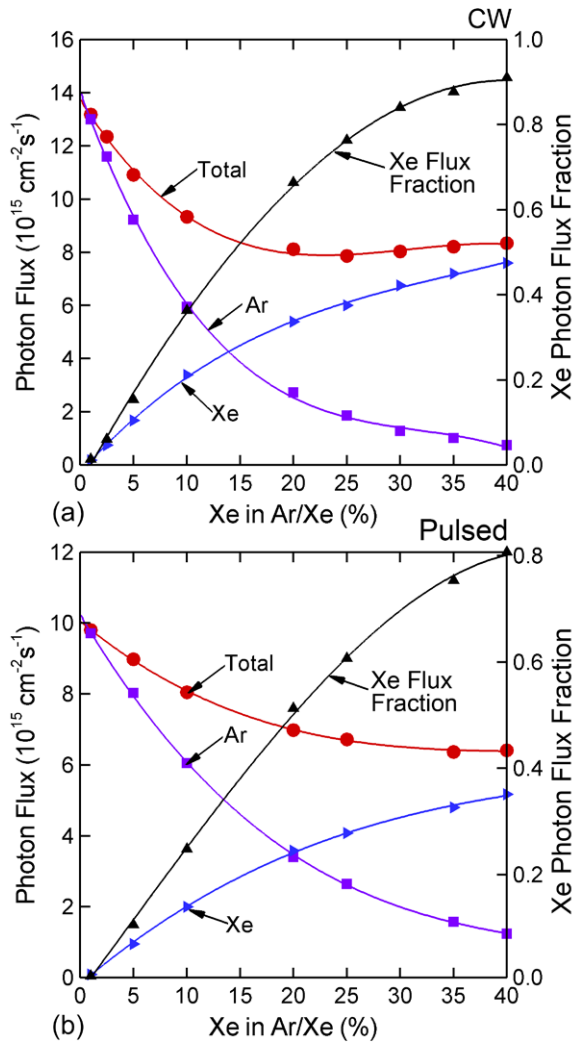


Figure 15. VUV fluxes as a function of Xe fraction in Ar/Xe mixtures for cw ICPs (20 mTorr, 200 sccm, 10 MHz, 150 W cw or CAP). (a) cw excitation, (b) pulsed excitation. The Ar flux is the sum of the 106.7 nm and 104.8 nm transitions. The Xe flux is the sum of 147 nm and 129.8 nm transitions. The total flux is the sum of VUV fluxes from both Ar and Xe.

self-absorbed as the Ar fraction decreases over this range. The lineshape function for 147.1 nm Xe emission becomes significantly more self-absorbed with increasing Xe fraction.

The control of spectrum in Ar/Xe mixtures was also investigated using pulsed power for a duty cycle of 15% and cycle-averaged power of 150 W. The VUV intensity from Xe and Ar, total VUV intensity and fraction of intensity due to Xe as a function of Xe fraction are shown in figure 15(b) for constant CAP and pressure. Qualitatively, the trends are similar to cw excitation—a decrease in total VUV flux with increasing Xe fraction and saturation in the VUV flux from Xe at a fraction of about 30%. The difference is that the fraction of the VUV flux due to Ar is larger than with cw excitation. For example, with 20% Xe, the fraction of the VUV flux due to Xe emission is 50%. For a Xe fraction of 40%, the fraction of VUV flux due to Xe emission is 80%. This decrease in the proportion of VUV emission due to Xe and increase in emission due to Ar results from the increase in T_e that occurs by pulsing power.

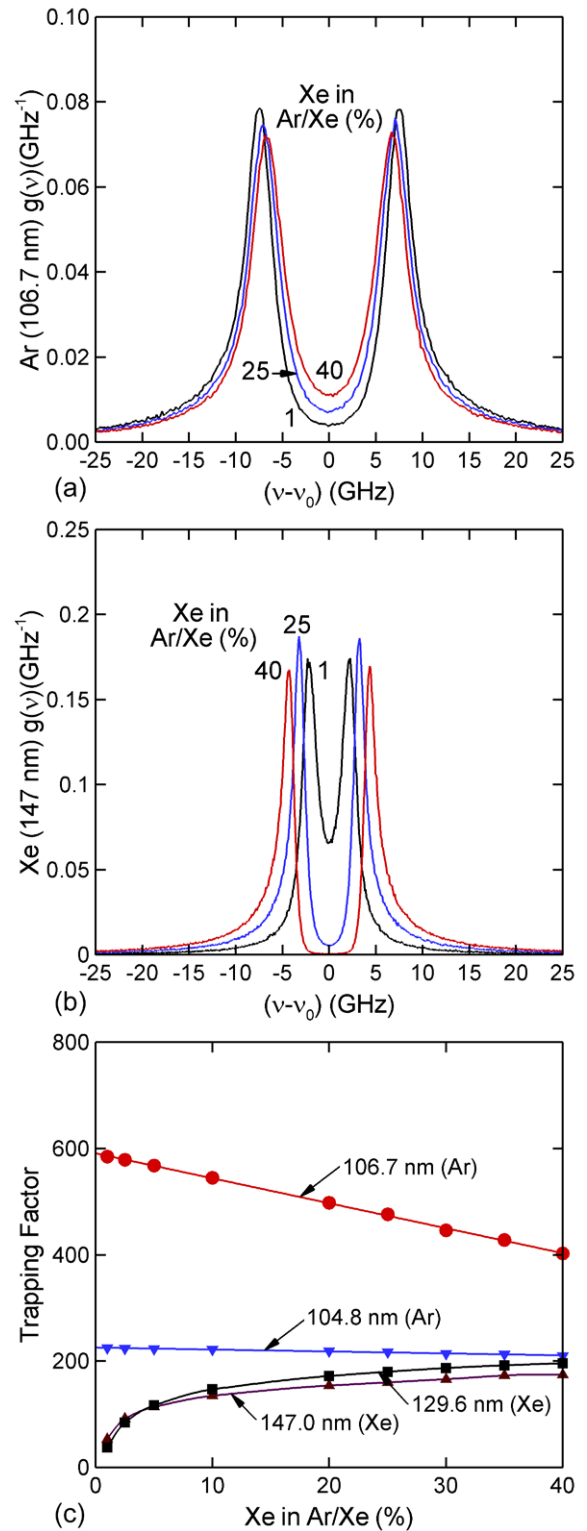


Figure 16. Optical properties for Ar/Xe ICPs for different fractions of Xe. (a) Lineshape function for 106.7 nm Ar emission, (b) lineshape for 147 nm Xe emission, and (c) radiation trapping factors for Ar and Xe emission.

(See, for example, figure 9 for pure argon.) Higher electron temperatures favor excitation of Ar compared to Xe due to the higher threshold energies for exciting Ar.

Control of the VUV spectrum was also investigated in He/Ar mixtures where VUV emission from He at 59.1 nm

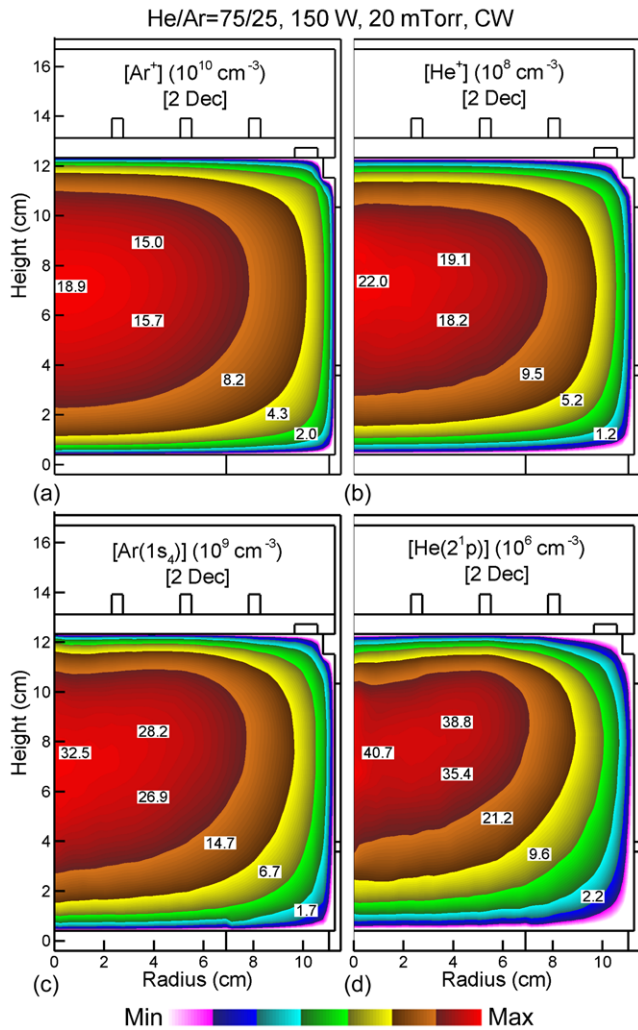


Figure 17. Plasma properties for an He/Ar = 75/25 mixture with cw excitation (20 mTorr, 200 sccm, 10 MHz, 150 W). (a) Ar^+ density, (b) He^+ density, (c) $Ar(1s_4)$ resonant state density, and (d) $He(2^1P)$ resonant state densities. The densities are plotted on 2-decade log scales.

adds a shorter-wavelength photon. The cw base case is He/Ar = 75/25, 20 mTorr and 150 W. The densities of Ar^+ , He^+ , $Ar(1s_4)$, and $He(2^1P)$ are shown in figure 17. The Ar^+ density is $1.9 \times 10^{11} \text{ cm}^{-3}$, 2 orders of magnitude larger than that of He^+ , $2.3 \times 10^9 \text{ cm}^{-3}$. The density of the radiating state $Ar(1s_4)$ is $3.4 \times 10^{10} \text{ cm}^{-3}$ and $He(2^1P)$ is $4.9 \times 10^7 \text{ cm}^{-3}$. These densities have similar disparities as the ion densities, with the He excited state density being 3 orders of magnitude lower than that for Ar.

EEDs for He/Ar mixtures at the edge of skin depth are shown in figure 14(b) for different Ar fractions. For small mole fractions of Ar the tail of the $f(\epsilon)$ extends well above 50 eV, an indication of the low stopping power of pure He plasmas. The cutoff at the ionization potential of He, 24.6 eV, is only minor. As the Ar fraction increases to as little as 10–20%, $f(\epsilon)$ assumes the two-temperature distribution associated with pure Ar discharges. T_e in the bulk and tail of $f(\epsilon)$ are 6.0 and 5.5 eV for 0.5% of Ar. T_e for the bulk and tail of $f(\epsilon)$ are 3.1 eV and 2.2 eV for 40% Ar.

In He/Ar mixtures, the vast majority of power is dissipated into Ar having the lower threshold energies, while all

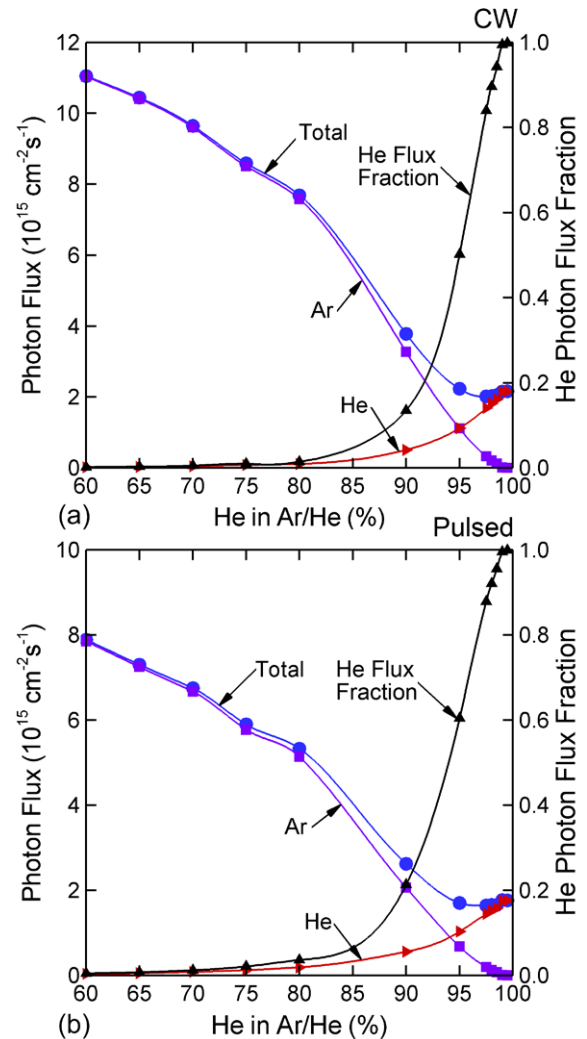


Figure 18. VUV fluxes as a function of He fraction in He/Ar mixtures for cw ICPs (20 mTorr, 200 sccm, 10 MHz, 150 W cw or CAP). (a) cw excitation, (b) pulsed excitation. The Ar flux is the sum of the 106.7 nm and 104.8 nm transitions. The He flux is the 59.1 nm transition. The total flux is the sum of VUV fluxes from both Ar and He.

excited states of He are capable of Penning-ionizing Ar. For example, based on collisions with the ground state, for an Ar/He = 50/50 mixture with an electron temperature of 4 eV, only 3% of the discharge power is dissipated by collisions with He, and the majority of those collisions are elastic. (These values were obtained from stationary solutions of Boltzmann's equation for the electron energy distribution.) The end result is that the vast majority of VUV emission from the plasma originates from Ar until large mole fractions of He. For example, the VUV flux originating from He and Ar, total VUV flux and fraction of VUV flux from He are shown in figure 18(a) as a function of He fraction. First, with increasing He fraction, the total VUV flux decreases. This is in large part a consequence of a smaller fraction of power being dissipated in exciting the radiative states with increasing He fraction. With trapping factors of 190–240 for VUV emission at 59.1 nm, the lifetime for $He(2^1P)$ is extended to 0.10–0.13 μs . With the rate coefficient for Penning ionization of $1 \times 10^{-9} \text{ cm}^3 \text{ s}^{-1}$, the frequency of

Penning ionization of Ar by He excited states is $2 \times 10^5 \text{ s}^{-1}$, or a lifetime of about $5 \mu\text{s}$. So resonant states of He are more likely to radiate than to be quenched by Penning collisions. However the lifetime for Penning collisions is much shorter than the rate of collisional mixing or radiative cascade that may populate $\text{He}(2^1\text{P})$ from higher levels. So a large fraction of the energy producing excited states of He is consumed by Penning processes before cascading to the $\text{He}(2^1\text{P})$. The Ar^+ produced by these processes then does not radiate. So power dissipated into excited states of He does not efficiently produce VUV emission compared to power dissipated into Ar.

The cross section for photoionization Ar ground state at 59.1 nm is $3.5 \times 10^{-17} \text{ cm}^2$ which produces a mean free path for these conditions of 30–100 cm. So there is only a moderate fraction of the 59.1 nm emission that is consumed by photoionization of Ar. The VUV emission from He/Ar mixtures is dominantly from Ar for mole fractions of Ar exceeding 5%. The VUV emission is 99% due to Ar for Ar mole fractions greater than 65%. The VUV emission is 99% due to He for He mole fractions exceeding 99%.

Trapping factors and VUV spectra from Ar at 106.7 nm and from He at 59.1 nm are shown in figure 19 for Ar mole fractions of 1% to 40%. For both mixtures, the He emission is heavily trapped. The trapping factor for 59.1 nm is 240 for He/Ar = 99.5/0.5 and 184 for He/Ar = 60/40. The self-absorption in the lineshape function is 3–4 times broader for He than for Ar due to the higher thermal speed of He. The lineshape function for Ar in the He/Ar = 99.5/0.5 mixtures shows little self-absorption and the trapping factor is 2.7. The 106.7 nm transition is essentially optically thin. For the He/Ar = 60/40 mixture, the trapping factor is 407 and the 106.7 nm transition is optically thick with self-absorption at line center.

The VUV fluxes originating from He, Ar, total VUV flux, and fraction of VUV flux from He are shown in figure 18(b) for pulsed power (duty cycle 15%) as a function of He fraction. The general trends for the pulsed ICP are similar to those for cw results. As was the case with Ar/Xe mixtures, when pulsing the higher T_e favors excitation of the atom with the higher threshold energies. Therefore, pulsing will produce more excited states and more ions in He compared to the same conditions for cw excitation. This produces more relative emission from He but less total emission. Quenching of He excited states channels more power into Ar^+ and less to VUV fluxes. So the total photon fluxes with pulsing are 27% lower than for cw excitation.

6. Concluding remarks

Results from a computational investigation suggest that VUV photon fluxes incident onto substrates in ICP reactors can be controlled to a certain extent. In pure Ar plasmas for constant power, the magnitudes of VUV photon fluxes onto the substrate are tunable by changing the gas pressure. However, the details of these trends depend on the details of the operating conditions and geometry of the reactor. In our base case, photon fluxes monotonically increased with pressure, asymptotically reaching a constant value at high

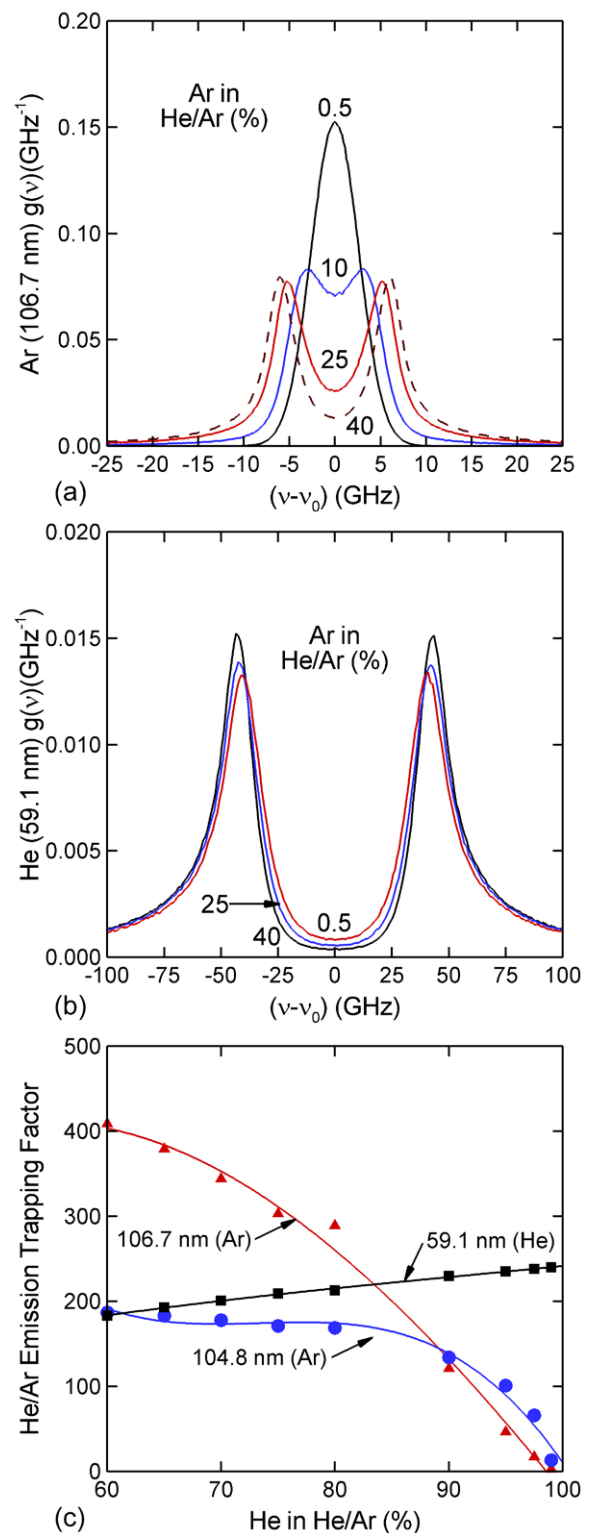


Figure 19. Optical properties for He/Ar ICPs for different fractions of Ar. (a) Lineshape function for 106.7 nm Ar emission, (b) lineshape for 59.1 nm He emission and (c) radiation trapping factors for Ar and He emission.

pressure. In this process, the increase in plasma density that typically occurs with increasing pressure produced a larger density of resonant states, which dominated over the adverse effects of more quenching and smaller view angle of the substrate to the source of VUV fluxes (the reduced view angle

resulted from the electron impact source for excited states being more confined to the skin depth). In contrast, in the work of Boffard *et al* [37] as well as in our corresponding simulations, VUV fluxes onto the substrate had a maximum at pressures of 10–15 mTorr. For this geometry, the increased quenching and reduced view angle of the substrate at higher pressures dominated over the increase in radiating-state densities.

Pulsing the ICP power allows for additional control over VUV photon fluxes. The rising edge of the power pulse will produce an overshoot of E/N , thus raising the tail of EEDs above the value occurring with cw excitation. Due to this overshoot, VUV fluxes onto the substrate have a larger peak value at lower duty cycles (larger overshoot of E/N), while the ion fluxes are less sensitive to duty cycle variations. The instantaneous ratios of VUV to ion fluxes are therefore sensitive functions of duty cycle.

The spectra of VUV photon fluxes can also be discretely tuned by changing the gas mixtures of the plasma. Two rare gas mixtures, Ar/Xe and He/Ar, were investigated. The rare gas component with the lower threshold energies for populating the resonant states will dominate the VUV spectra until the higher-threshold gas has a large mole fraction. The efficiency of total VUV photon production was higher for large mole fractions of Ar in both mixtures. In Ar/Xe mixtures, a larger proportion of energy is expended in ionizing Xe compared to excitation when the Xe fraction is increased. In He/Ar mixtures, through Penning reactions, electronic excitation of He produces ground-state Ar⁺ which does not directly radiate. So although one gains the ability to tune the VUV spectra in these mixtures, that advantage is offset by a decrease in efficiency of VUV production.

Acknowledgments

This work was supported by the Semiconductor Research Corp., the Department of Energy Office of Fusion Energy Science (DE-SC0001319), the National Science Foundation (CHE-1124724), and Agilent Technologies.

References

- [1] Wang S-B and Wendt A E 2001 *J. Vac. Sci. Technol. A* **19** 2425
- [2] Athavale S D and Economou D J 1995 *J. Vac. Sci. Technol. A* **13** 966
- [3] Schaepkens M, Oehrlein G S and Cook J M 2000 *J. Vac. Sci. Technol. B* **18** 848
- [4] Barela M J, Anderson H M and Oehrlein G S 2005 *J. Vac. Sci. Technol. A* **23** 408
- [5] Banna S *et al* 2009 *IEEE Trans. Plasma Sci.* **37** 1730
- [6] Agarwal A, Stout P J, Banna S, Rauf S and Collins K J 2011 *J. Vac. Sci. Technol. A* **29** 011017
- [7] Xu L, Economou D J, Donnelly V M and Ruchloeft P 2005 *Appl. Phys. Lett.* **87** 041502
- [8] Lee H S, Tiwari P K and Lee J K 2009 *Plasma Source Sci. Technol.* **18** 025024
- [9] Qin V X, Ting Y-H and Wendt A E 2010 *Plasma Sources Sci. Technol.* **19** 065014
- [10] Diomede P, Economou D J and Donnelly V M 2011 *J. Appl. Phys.* **109** 083302
- [11] Hwang G S and Giapis K P 1997 *J. Vac. Sci. Technol. B* **15** 70
- [12] Gottscho R A, Jurgensen C W and Vitkavage D J 1992 *J. Vac. Sci. Technol. B* **10** 2133
- [13] Schaepkens M and Oehrlein G S 1998 *Appl. Phys. Lett.* **72** 1293
- [14] Woodworth J R, Blain M G, Jarecki R L, Hamilton T W and Aragon B P 1999 *J. Vac. Sci. Technol. A* **17** 3209
- [15] Woodworth J R, Riley M E, Amatucci V A, Hamilton T W and Aragon B P 2001 *J. Vac. Sci. Technol. A* **19** 45
- [16] Jinnai B, Fukuda S, Ohtake H and Samukawa S 2010 *J. Appl. Phys.* **107** 043302
- [17] Titus M J, Nest D and Graves D B 2009 *Appl. Phys. Lett.* **94** 171501
- [18] Lee J and Graves D B 2010 *J. Phys. D* **43** 425201
- [19] Uchida S, Takashima S, Hori M, Fukasawa M, Ohshima K, Nagahata K and Tatsumi T 2008 *J. Appl. Phys.* **103** 073303
- [20] Nest D, Graves D B, Engelmann S, Bruce R L, Weilboeck F, Oehrlein G S, Andes C and Hudson E A 2008 *Appl. Phys. Lett.* **92** 153113
- [21] Titus M J, Graves D B, Yamaguchi Y and Hudson E A 2011 *J. Phys. D: Appl. Phys.* **44** 085204
- [22] Shin H, Zhu W, Donnelly V M and Economou D J 2012 *J. Vac. Sci. Technol. A* **30** 021306
- [23] Lerouge S, Fozza A C, Wertheimer M R, Marchand R and Yahia L H 2000 *Plasma Polym.* **5** 31
- [24] Herd M T, Lawler J E and Menningen K L 2005 *J. Phys. D: Appl. Phys.* **38** 3304
- [25] Kushner M J 2009 *J. Phys. D: Appl. Phys.* **42** 194013
- [26] Scharfetter D L and Gummel H K 1969 *IEEE Trans. Electron Devices* **ED-16** 64
- [27] Song S-H and Kushner M J 2012 *Plasma Sources Sci. Technol.* **21** 055028
- [28] Weibel E S 1967 *Phys. Fluids* **10** 741
- [29] Kolobov V I and Economou D J 1997 *Plasma Sources Sci. Technol.* **6** R1
- [30] Tyshetskiy Y O, Smolyakov A I and Godyak V A 2003 *Phys. Rev. Lett.* **90** 255002
- [31] Rauf S and Kushner M J 1997 *J. Appl. Phys.* **81** 5966
- [32] Menningen K L and Lawler J E 2000 *J. Appl. Phys.* **88** 3190
- [33] Lawler J E and Raizen M G 2013 *J. Phys. D: Appl. Phys.* **46** 415204
- [34] Parker G J, Hitchon W N G and Lawler J E 1993 *J. Phys. B: At. Mol. Opt. Phys.* **26** 4643
- [35] Lawler J E, Curry J J and Lister G G 2000 *J. Phys. D: Appl. Phys.* **33** 252
- [36] Holstein T 1947 *Phys. Rev.* **72** 1212
- [37] Boffard J B, Lin C C, Culver C, Wang S, Wendt A E, Radovanov S and Persing H 2014 *J. Vac. Sci. Technol. A* **32** 021304
- [38] Hopwood J, Guarnieri C R, Whitehair S J and Cuomo J J 1993 *J. Vac. Sci. Technol. A* **11** 152
- [39] Godyak V A, Piejak R B and Alexandrovich B M 2002 *Plasma Sources Sci. Technol.* **11** 525
- [40] Ashida S, Shim M R and Lieberman M A 1996 *J. Vac. Sci. Technol. A* **14** 391
- [41] Ahn T H, Nakamura K and Sugai H 1996 *Plasma Sources Sci. Technol.* **5** 139
- [42] McCann K J and Flannery M R 1977 *Appl. Phys. Lett.* **31** 599
- [43] Lawrence G M 1968 *Phys. Rev.* **175** 40
- [44] Dyatko N A, Ionikh Y Z, Kochetov I V, Marinov D L, Meshchanov A V, Napartovich A P, Petrov F B and Starostin S A 2008 *J. Phys. D.* **41** 055204
- [45] Kannari F, Obara M and Fujioka T 1985 *J. Appl. Phys.* **57** 4309
- [46] Hayashi M 1991 Report No. IPPJ-AM-19 Nagoya Institute of Technology

- [47] Petrov G M, Giuliani J L and Dasgupta A 2002 *J. Appl. Phys.* **91** 2662
- [48] Rapp D and Englander-Golden P 1965 *J. Chem. Phys.* **43** 1464
- [49] Bogaerts A, Gijbels R and Vlcek J 1988 *J. Appl. Phys.* **84** 121
- [50] Vlcek J 1989 *J. Phys. D* **22** 623
- [51] Vriens L 1964 *Phys. Lett.* **8** 260
- [52] Biondi M A 1976 *Principles of Laser Plasmas* ed G Bekefi (New York: Wiley) (ch 4)
- [53] Ellis W W, Pai R Y, McDaniel E W, Mason E A and Viehland L A 1976 *At. Data Nucl. Data Tables* **17** 177
- [54] Bogaerts A and Gijbels R 1999 *J. Appl. Phys.* **86** 4124
- [55] Becker P M and Lampe F W 1965 *J. Chem. Phys.* **42** 2857
- [56] Johnsen R, Chen A and Biondi M A 1980 *J. Chem. Phys.* **73** 1717
- [57] Lukac P, Mikus O, Morva I, Zabudla Z, Trnovec J and Morvova M 2011 *Plasma Source Sci. Technol.* **20** 055012
- [58] www.nist.gov/pml/data/asd.cfm
- [59] Ohwa M, Moratz T J and Kushner M J 1989 *J. Appl. Phys.* **66** 5131
- [60] Hokazono H, Midorikawa K, Obara M and Fujioka T 1984 *J. Appl. Phys.* **56** 680
- [61] Biagi-v8.9 Database, www.lxcat.net, retrieved on July 2, 2012
- [62] Deloche R, Monchicourt P, Cheret M and Lambert F 1976 *Phys. Rev. A* **13** 1140
- [63] Niemi K, Waskoenig J, Sadeghi N, Gans T and O'Connell D 2011 *Plasma Sources Sci. Technol.* **20** 055005
- [64] Johnson A W and Gerardo J B 1972 *Phys. Rev. A* **5** 1410
- [65] Miller T J, Farquhar P R A and Willacy K 1997 *Astron. Astrophys. Suppl. Ser.* **121** 139
- [66] Emmert F, Angermann H H, Dux R and Langhoff H 1988 *J. Phys. D* **21** 667
- [67] Lindinger W, Schmeltekopf A L and Fehsenfeld F C 1974 *J. Chem. Phys.* **61** 2890
- [68] Schmeltekopf A L and Fehsenfeld F C 1970 *J. Chem. Phys.* **53** 3173
- [69] Jones J D C, Lister D G and Twiddy N D 1979 *J. Phys. B* **12** 2723
- [70] Fehsenfeld F C, Schmeltekopf A L, Goldan P D, Schiff H I and Ferguson E E 1966 *J. Chem. Phys.* **44** 4087
- [71] Bohme D K, Adams N G, Mosesman M, Dunkin D B and Ferguson E E 1970 *J. Chem. Phys.* **52** 5094
- [72] Lorents D C, Eckstrom D J and Huestis D 1973 Excimer and decay processes in rare gases *Report No. N00014-72-C-0457*, Sept. Stanford Research Institute
- [73] Gnybida M, Uhrlandt D, Loffhagen D 2012 *J. Phys. D: Appl. Phys.* **45** 195203